JGR Solid Earth

RESEARCH ARTICLE

10.1029/2018JB017023

Key Points:

- Seismicity originates at the summit crater
- We compare array and amplitude location methods
- Near-surface *S* wave velocities, from surface wave dispersion measurements, are consistent with volcanic deposits

Supporting Information:

- Supporting Information S1

Correspondence to:

J. Lehr,
johanna.lehr@ifg.uni-kiel.de

Citation:

Lehr, J., Eckel, F., Thorwart, M., & Rabbel, W. (2019). Low-frequency seismicity at Villarrica Volcano: Source location and seismic velocities. *Journal of Geophysical Research: Solid Earth*, *124*, 11,505–11,530. https://doi.org/10.1029/2018JB017023

Received 12 NOV 2018
Accepted 27 SEP 2019
Accepted article online 15 OCT 2019
Published online 7 NOV 2019

Low-Frequency Seismicity at Villarrica Volcano: Source Location and Seismic Velocities

Johanna Lehr[1], **Felix Eckel**[1], **Martin Thorwart**[1], **and Wolfgang Rabbel**[1]

[1]Institute of Geosciences, Kiel University, Kiel, Germany

Abstract Villarrica Volcano (Chile) is one of the most active volcanoes in South America. Its low-frequency (≤5 Hz) seismicity consists of a continuous tremor, overlain by impulsive transient events of higher amplitude in 60-s intervals. This signal was recorded in March 2012 by an extensive local network, comprising 75 stations and including 6 subarrays. It allowed us to apply and compare three techniques to locate the origin of the seismicity: intersection of propagation directions determined by array analysis, mapping amplitudes, and modeling of amplitude decay. All methods yield almost identical, temporally stable, epicenters inside the summit crater, which confirms earlier attributions of the seismicity to volcanic activity inside the conduit. The discrete transients and the interevent tremor share the same source location. From the dominance of surface waves and the obvious scattering, we infer a source near the surface. For two arrays at the northern and western flank, a dispersion relation was derived, which allowed for the determination of *S* wave velocity-depth functions. At both locations, the velocity structure can be modeled by three layers with interfaces at 100 and 400m depths. The velocities (300 to 3,000 m/s) correspond to pyroclastic material at different states of consolidation. The modeling of the amplitude decay reveals a quality factor around 50.

1. Introduction

Villarrica is a 2,847-m-high, glacier-covered stratovolcano of basaltic to basaltic-andesitic composition in the Chilean Andes. It is considered one of the most active and dangerous volcanoes in South America with lahars posing the largest threat to the local population (≈35,000 persons within 30 km) and the numerous tourists of the national park. The last 30 years have been marked by a sustained mild level of activity including an active lava lake, which feeds mild strombolian eruptions and lava effusion, occasional explosions and scoria ejections, and continuous degassing. This activity mostly affects only the crater region. The latest larger eruption occurred in March 2015. It caused several lahars at the northwestern flank, an ash plume of 3-km height and a lava fountain reaching 1.5 km (Global Volcanism Program, 2015).

The volcanic activity is accompanied by a persistent tremor of 0.5–5.0 Hz. For extended periods of days to weeks, it may be overlain by transient, high-amplitude events, which are attributed to strombolian explosions (Calder et al., 2004; Ortiz et al., 2003; Palma et al., 2008). A similar signal is observed in the infrasonic spectrum (Goto & Johnson, 2011; Richardson et al., 2014; Ripepe et al., 2010). The entirety of the signal has been denoted by previous authors as "tremor" (Ortiz et al., 2003; Palma et al., 2008; Ripepe et al., 2010), while the impulsive bursts were termed "strombolian explosions" (Calder et al., 2004; Ortiz et al., 2003), "discrete, higher-amplitude bursts," "high-amplitude transients" (Palma et al., 2008), or "long-period (LP) events" (Richardson & Waite, 2013). This mix of terminology reflects the lack of detailed knowledge concerning the nature of the seismicity. For example, few studies specifically address the issue of locating the source of the seismic signal. Ripepe et al. (2010) used a small array of infrasonic sensors to attribute the infrasonic tremor to the crater. From the similarity of infrasonic and seismic signal they deduced a common origin. Richardson and Waite (2013) applied a waveform inversion to a single, repetitive "LP" event and located its source at shallow depth inside the conduit.

The continuity of the tremor and the lack of clear event onsets inhibit the application of conventional location methods. To overcome these typical limitations for volcanic signals, a number of alternative approaches have been developed. Array-based techniques have been successfully applied to locate discrete, emergent events—such as LP events (Almendros et al., 2001a; Chouet et al., 1997; Saccorotti et al., 2001)—as well as continuous tremor (Di Lieto et al., 2007; Eibl et al., 2017; Métaxian et al., 1997, 2002). Multiple small arrays allow to determine the epicenter without a velocity model by intersecting the backprojected backazimuths (e.g., Métaxian et al., 2002). With an accurate velocity model at hand, more sophisticated methods, which refine the determination of the slowness vector by comparison with simulated parameters, significantly reduce the uncertainty of the location and even enable the determination of the source depth (Almendros et al., 2001a; Wassermann, 1997). Inherently, array methods provide information on the subsurface velocity structure. If the frequency-dependent phase velocity of surface waves can be determined, this dispersion relation can be inverted for a shallow velocity model. In early attempts by Chouet et al. (1998) and Métaxian et al. (1997) regularly spaced, semicircle arrays were deployed to make use of the spatial autocorrelation (SPAC) method introduced by Aki (1957), whereas Zuccarello et al. (2016) and Saccorotti et al. (2001) used irregular arrays and a modified version of SPAC.

An entirely different approach was proposed by Battaglia (2003). They located LP and other events at Kilauea (Hawaii) and Piton de la Fournaise (La Reunion) first by interpolating the amplitudes within the sensor network and second by inverting for the amplitude-distance relation of the decaying amplitude. The decay is controlled by geometrical spreading and intrinsic attenuation (see, e.g., Aki & Richards, 2002; Stein & Wysession, 2009). Since the latter has a considerable effect on the result (Kumagai et al., 2010), the method provides also an estimate of the attenuation coefficient of the medium. The method is applicable to surface waves as well as body waves

Numerous variations of these techniques have been applied in the last two decades—along with different approaches such as the combination of particle motion with semblance analysis for very long period events (Almendros & Chouet, 2003; Zuccarello et al., 2013) or the use waveform inversion (e.g., Ohminato et al., 1998) or cross correlation (e.g., De Barros et al., 2009).

The main objective of this paper is to locate the origin of the low-frequency seismicity at Villarrica Volcano. To that purpose, we use data of a dense temporary sensor network, which was deployed in March 2012—originally intended for a velocity tomography (Mora-Stock, 2015). The abundance of stations on and around the volcano makes the network predestined for the application of the amplitude source location method. In addition, the network comprised six subgroups, which we used for array analysis. In the present study, we compare the location results obtained by both approaches. We do not distinguish between events and tremor but look at the seismicity in its entirety. However, we examine the temporal variation of the epicentral zone. As pointed out above, both location techniques provide also information on *S* wave velocities and average attenuation of the subsurface. Contrary to other authors, who used the SPAC method to derive a dispersion relation for surface wave inversion (e.g., Ferrazzini et al., 1991; Métaxian et al., 1997; Saccorotti et al., 2001; Zuccarello et al., 2016), we directly use the slowness-frequency functions obtained from the array analysis. As of today, the knowledge about the seismic structure of Villarrica is sparse. Hence, our results may provide a valuable base for future more detailed work including numerical simulations.

The paper is organized as follows. In the next sections, we introduce the geology and the technical details of the data acquisition campaign, followed by an overview of the seismic and volcanic activity during that time. Subsequently, we explain the array and the amplitude-based methods including the determination of the velocity structure. Sections 6, 7, 8, 6.1 6.2, 7.1,7.2, 7.3, and7.4 contain the results, discussion, and conclusion, respectively.

2. Geology of Villarrica Volcano

Villarrica Volcano is a 2,847-m-high stratovolcano located about 700 km south of Santiago in Southern Central Chile (Figure 1, top left). It is situated above the subducting oceanic Valdivia fracture zone, the fluid release from which is thought to feed the magmas of the Villarrica system (Dzierma et al., 2012). The volcano is composed of basaltic to basaltic-andesitic rocks. Its edifice consists of two larger, collapsed calderas (about 6-km diameter) that formed during the Pleistocene (Moreno & Clavero, 2006). At their western rim, the current cone is situated in a younger (3.5 ka, Global Volcanism Program, 2013), smaller caldera (about 2-km diameter). It hosts a summit crater of about 200-m diameter and an active lava lake with a varying depth of 50–250 m below the crater rim (Richardson et al., 2014). A glacier covers the upper 1,000 m of the volcano. Volcanic activity consists of mild strombolian eruptions and lava effusion, occasional mild-to-moderate explosions, and ash/scoria ejections as well as continuous degassing. Its high activity and the proximity to human settlements make it one of the most dangerous volcanoes in Chile. Significant deposits were produced by three violent explosive eruptions during the Holocene. From the Lícan eruption (13.9 ka), up to

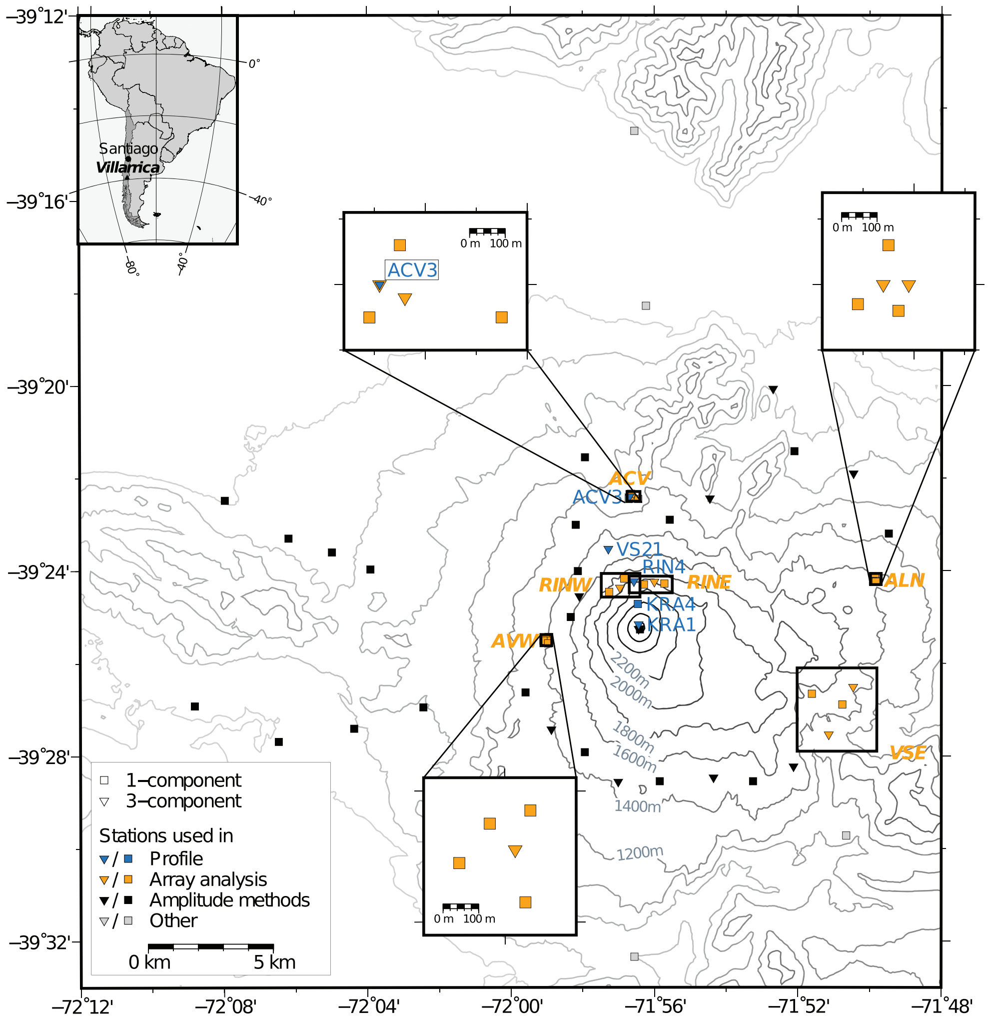

Figure 1. Topography and seismic station setup. Symbol shapes represent the instrument type while black, blue, and orange colors indicate what the station was used for in this paper. Gray stations were not used in this study. Subarrays used for beamforming are outlined by boxes. Subarrays ACV, ALN, and AVW are enlarged in extra boxes.

25 m thick, exposed layers of ignimbrites were found (Lohmar et al., 2007, 2012), while the Pucón ignimbrites (3.5 ka) reach up to 70 m (Parejas et al., 2010). The Chaimilla eruption (3.1 ka) deposited up to 2.5 m of material (Costantini et al., 2011). These ignimbrites consist mostly of alternating layers of ash, scoria, lapilli, and volcanic bombs, deposited by fallout or pyroclastic flows. The Lícan (Lohmar et al., 2012) and Chaimilla (Costantini et al., 2011) ignimbrites are found predominantly to the west and northwest of the volcano, respectively, while the Pucón deposits (Parejas et al., 2010) are widespread around the edifice.

3. Seismic Data Acquisition

3.1. Network

A network of 75 short-period stations was deployed in an area of approximately 63 km × 55 km around Villarrica Volcano between 1 and 14 March 2012 (Rabbel & Thorwart, 2019). It was designed for exploring the *P* wave velocity structure in a previous study (Mora-Stock, 2015). The 58 stations used in this paper for determining the origin of the seismicity are shown in Figure 1 in black, blue, and orange—depending on the method.

The stations consisted of a DSS-Cube and a SM-6/U 4.5-Hz geophone from the Geophysical Instrument Pool Potsdam of the GeoForschungsZentrum Potsdam (Germany). Thirty stations were equipped with three-component (3C) and 45 with one-component (1C) sensors. The instrument type is represented by the symbol shape in Figure 1. The operation time of each station is depicted in Figure 13 in the supporting information. The instrument response was removed using a four-corner band-pass prefilter of (0.3, 0.4, 30, 45 Hz) and a waterlevel of 40. We verified in a laboratory experiment—following Havskov and Alguacil (2004), Pavlis and Vernon (1994), and Wielandt and Bormann (2002)—that the bandwidth of these sensors can reliably be extended to one or even two decades below their nominal natural frequency by removing the instrument response (Hilbert, 2015). To demonstrate this beneficial effect of the instrument correction on the bandwidth, we included examples from the laboratory study and a filter example using field data from this study in the supporting information (section S1). All data were filtered using a strict lower cutoff frequency of 0.5 Hz before any further analysis.

About 50 stations were situated within a radius of 10 km around the summit. Three stations (KRA1–KRA3) were installed at the crater rim (2,800 m above sea level), seven (RIN1–RIN7) were deployed on the northern flank at a height of approximately 1,800 m above sea level and 24 were distributed around the volcano on the 1,500-m contour line. Additionally, three groups of five stations (AVW, ACV, and ALN) were installed as subarrays to the west, north, and east of the summit (insets in Figure 1). The glacier is roughly outlined by the 1,800 contour line showing that only Stations KRA1-4 and RIN1-7 were installed within or near the glacier.

3.2. Subarray Setup

For the present study, three smaller subarrays (AVW, ACV, and ALN) were used as antennas for beamforming together with three spatially larger subgroups of seismometers located at the rim and southeast of the crater (RINW, RINE, and VSE). Stations belonging to the subarrays are colored in orange in Figure 1, whereas groups are surrounded by black boxes.

The three subarrays AVW, ACV, and ALN consisted of five stations each with a maximum aperture of 300, 300, and 200 m, respectively, and a mean station spacing of approximately 100 m. They were situated to the west, north, and east of the summit in distances of 4, 6, and 10 km, respectively. The RIN stations were divided into two linear arrays RINW and RINE, comprising the stations RIN1-4 and RIN4-7. The distance to the summit was about 2 km, and the spacing between the stations was about 400 m. This resulted in a maximum aperture of 1.5 km for each subarray toward the summit. The last subarray consisted of the stations VS12-15, which were located to the southeast of the summit in a distance of 8–9 km. These stations also had a fairly large spacing of 900–1,500 m, resulting in a maximum aperture of 2.5 km. The records of the small arrays AVW, ACV, and ALN show coherent signals at frequencies up to 4 Hz, whereas RINE, RINW, and VSE show coherent records only up to about 2 Hz because of the larger station spacing.

RINE and RINW were very close to the expected source region, so that the plane wave front assumption was no longer strictly fulfilled. However, test computations with plane and circular wavefronts showed that the resulting deviation of beam directions are less than 3°, which appears tolerable.

3.3. Volcanic Activity

The seismic campaign took place during a period of relative quiescence in volcanic activity (Global Volcanism Program, 2014). The last strombolian activity before the campaign was reported on 26 September 2011, followed by a period with almost no explosive activity until March 2012. During our campaign, two small ash emissions were observed on 7 March, incandescence from the lava lake on 7 and 8 March and lava spattering from 7 to 9 March. Shortly afterward, another four small ash emissions occurred during 13–14 March, succeeded by a large white plume on 20 March and an 50-m-high ash plume on 19 April. Incandescence ceased during April and was not observed until at least November. Analysis of infrared satellite data by MODVOLC (Wright et al., 2004) revealed an elevated level of thermal radiance that started in early 2010 and ended shortly after the previously described activity in 2012. Incandescence and thermal anomalies indicate that the lava lake is active. Significant activity was not resumed until the end of September 2014.

3.4. Low-Frequency Seismic Activity

The seismicity was dominated by a persistent low-frequency signal throughout the whole observation time. The waveforms varied between a diffuse tremor of relatively uniform intensity over longer time spans (>60 s) and sections with high-amplitude transient signals. Examples of these two extreme cases are shown in the first 400 s of Figure 2, top, and Figure 2, bottom, respectively. For lack of detailed knowledge about the true nature of the events and tremor, we employ the rather generic terms tremor and “transient events” as suggested by Palma et al. (2008). Most of the time, the signal consisted of a mixture

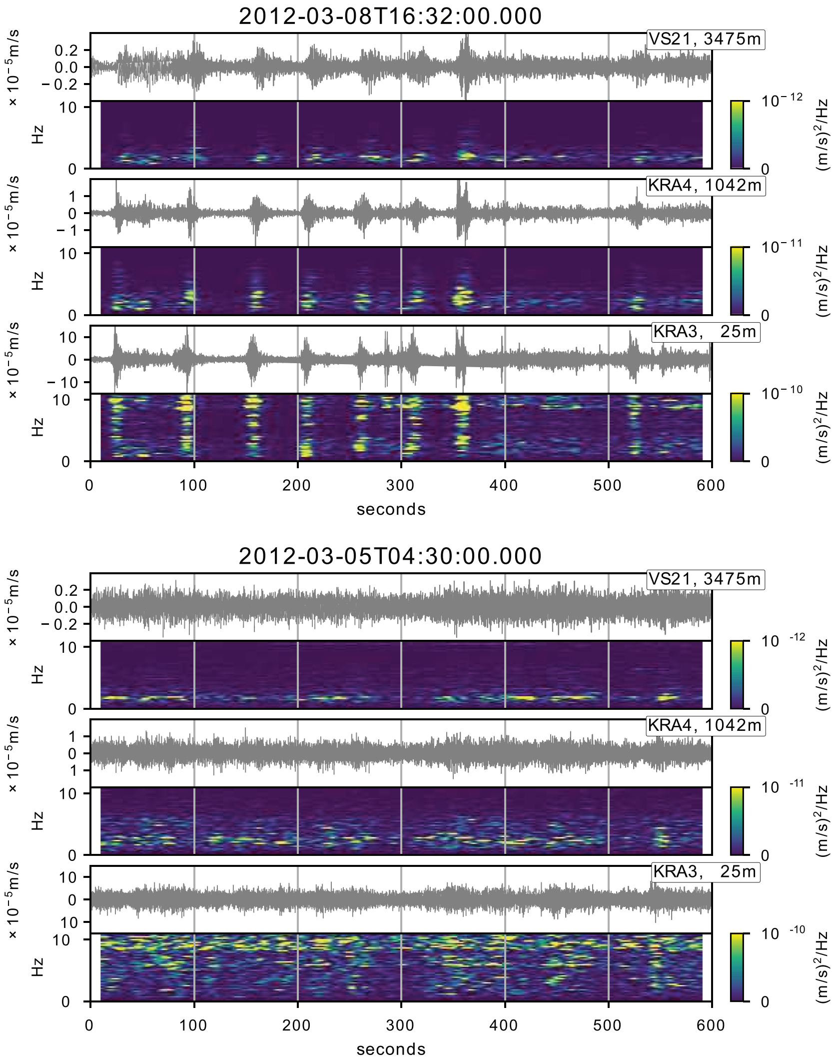

Figure 2. Samples of the two end-members of the tremor/event mix: (top) Distinct, impulsive transients, embedded in a low background tremor level during the first 400 s. (bottom) High tremor level with no or barely visible events. Frequency: 0.5–25.0 Hz, sampling rate: 50 Hz, spectrogram: 20.48 s with 20-s overlap, indicated distance is to source location at the summit.

thereof, which is periodic transients separated by a relatively high level of background activity (Figure 2, bottom, $t \geq 400$ s). The corresponding spectrograms show that the frequency range varies with distance to the crater. At the crater rim, the signal energy is distributed between 0.5 and 10 Hz, whereas it is concentrated to the 0.5- to 2-Hz band at distances larger than 3 km. Station VS21 was situated similarly to the stations used in the earlier studies of Ortiz et al. (2003), Calder et al. (2004), and Palma et al. (2008). Here, the energy peak lies at about 2 Hz, which is consistent with previously reported ranges. Figure 3, top, shows transient events in a 1-hr-long record section of Station VS21. The comparison to the earlier studies (data from October 2000, March 2000, and February 2005, respectively) revealed a quite similar character of the seismicity with transients occurring about every 60 s.

As shown in Figure 3, bottom, these bursts showed emergent onsets and spindle-shaped, elongated waveforms at most stations (upper four traces). These features are frequently associated with LP events (Chouet, 1996). Near the crater (<500 m), however, the waveforms were significantly shorter and more impulsive. Additionally, they contained much higher frequencies up to 10 Hz or more. Thus, the event waveforms showed a significant alteration and elongation along their travel path, indicating a strong influence of scattering effects. The same phenomenon was already observed by Richardson and Waite (2013). In particular, they noted the possibility of falsely interpreting the discrete events as tremor if they were observed

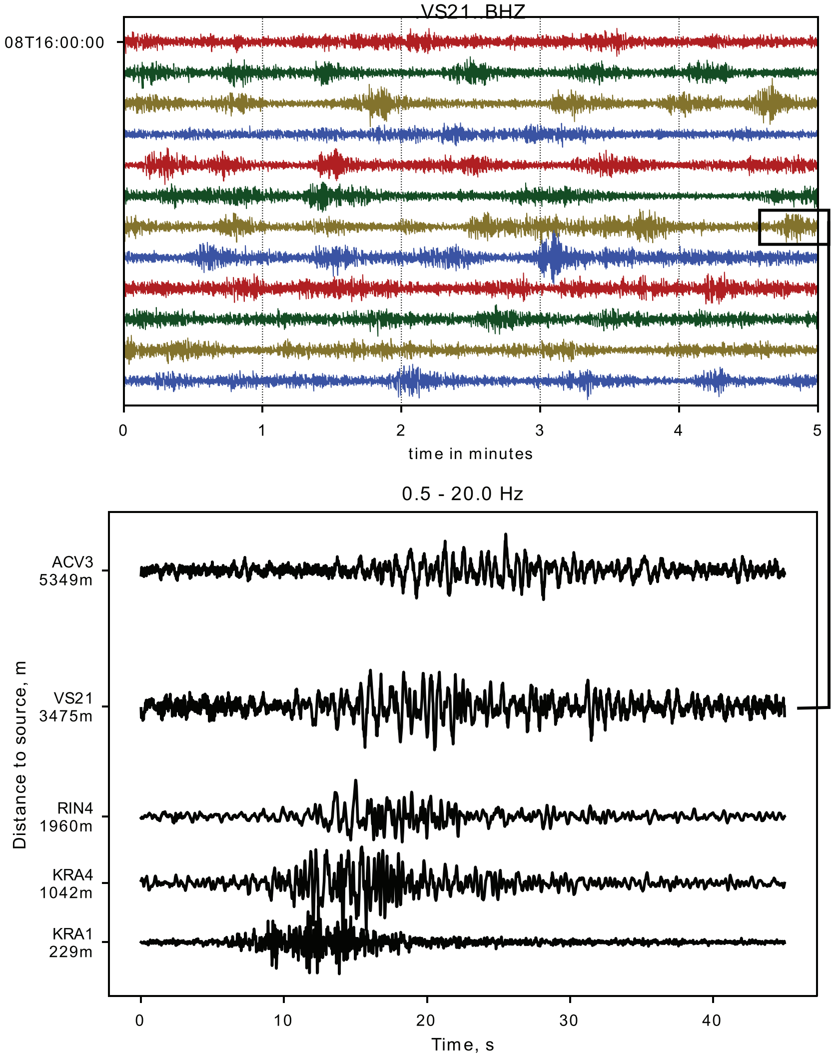

Figure 3. Transient events; signal is filtered between 0.5 and 20.0 Hz. (top) Occurrences in 1-hr section of Station VS21. bottom: Evolution of a single event with distance to the source on vertical component: Amplitudes are normalized to the respective trace maximum. The spacing between the traces corresponds to horizontal distance between stations. The waveform originates at the summit and propagates along the northern flank.

only at late stations. The spectral content of the transients and the background unrest was similar and stable throughout the period of observation at each station. Additional record sections and spectrograms are provided in the supporting information.

4. Source Location by Probabilistic Slowness Analysis ("Array Analysis")

4.1. Beamforming

A group of at least three relatively closely spaced stations can serve as an antenna to detect the direction of arrival (DOA) and the horizontal slowness (inverse horizontal velocity) of an incoming wavefield. A plane wave, which crosses this group, produces the same waveform at each station, only slightly shifted in time (Figure 4). The set of pairwise time shifts is determined by the DOA and the propagation velocity of the wavefront. As long as the wavefield maintains its coherency across the antenna, the time shifts are easy to detect. The corresponding slowness vector is usually found by a systematic grid search, which can be implemented in the time or frequency domain. The waveforms are shifted in time according to the test vector and stacked (beamforming or beampacking). The most suitable vector yields the highest power. Detailed explanation on the principles of array analysis and implementation of how to determine the slowness vector can be found, for example, in Schweitzer et al. (2012).

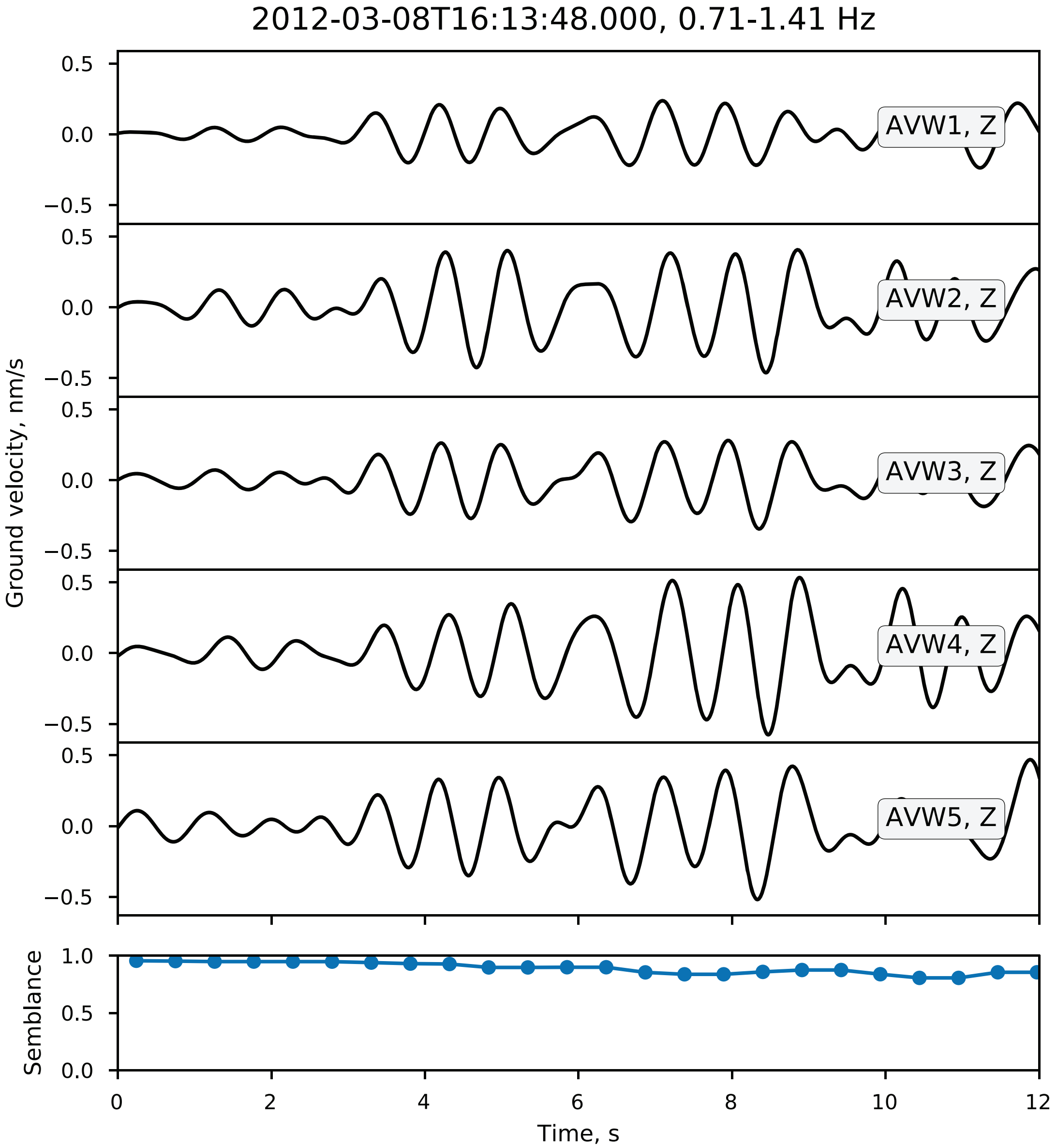

Figure 4. Coherent waveforms during a transient event within Subarray AVW. Data were filtered between 0.71 and 1.41 Hz. Corresponding semblance values (lowest panel) are drawn at the beginning of each 5.12-s analysis window.

We applied the frequency-wavenumber analysis implemented in ObsPy (The ObsPy Development Team, 2017). The quality of the stacked signal is measured by the semblance coefficient, which is a dimensionless quantity between 0 (no coherency) and 1 (perfect coherency). The analysis was applied to 1-h sections, which were divided into successive time windows of 5.12 s with an overlap of 90%. The arrays operated from 2012-03-04T00:00:00 to 2012-03-13T00:00:00. For subarrays ALN and ACV two hours are missing due to numerical issues with the data. We tested 61 slowness values between 0.05 and 3.0 s/km (corresponds to 0.3–20 km/s). DOAs were sampled in intervals of 2° between 0° and 360°. The output consisted of time series of the maximum semblance as well as the corresponding DOA and slowness values. In addition, we computed the absolute energy content of the stacked signal. Following Almendros et al. (2001b), we quantified the uncertainty of the DOA and slowness by determining the extent of the 95%-of-the-maximum-region in both slowness dimensions. We chose five frequency bands of one octave between 0.5 and 4.0 Hz, overlapping each other by one half octave.

Figure 5 shows the time series of all three parameters for three frequency bands during two consecutive episodic events. Evidently, high semblance values are achieved not only during events but also during

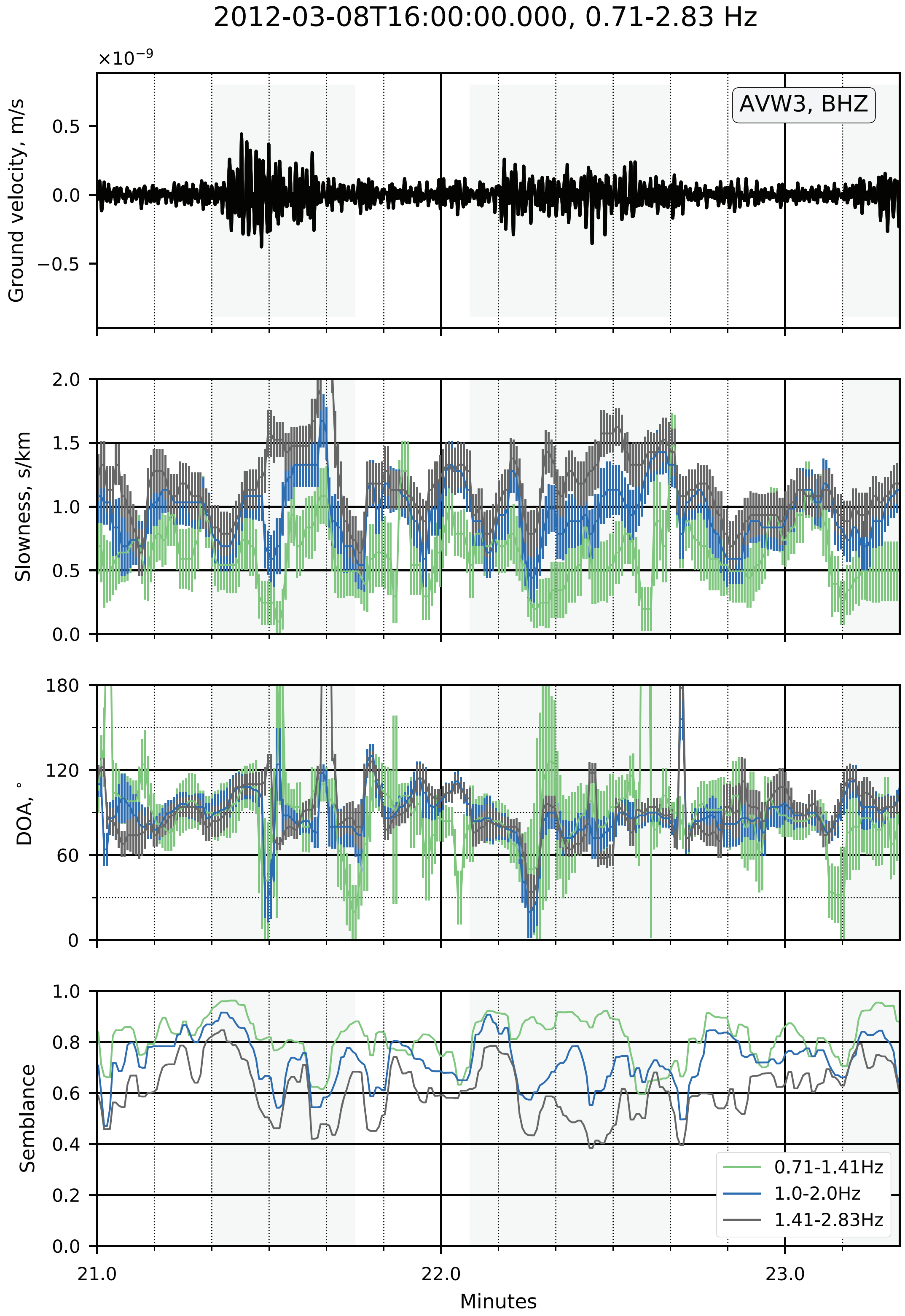

Figure 5. Time series of beamforming results for signal (top) at AVW: Transient events are shaded in gray. Parameters vary independently of event occurrences. DOA = direction of arrival.

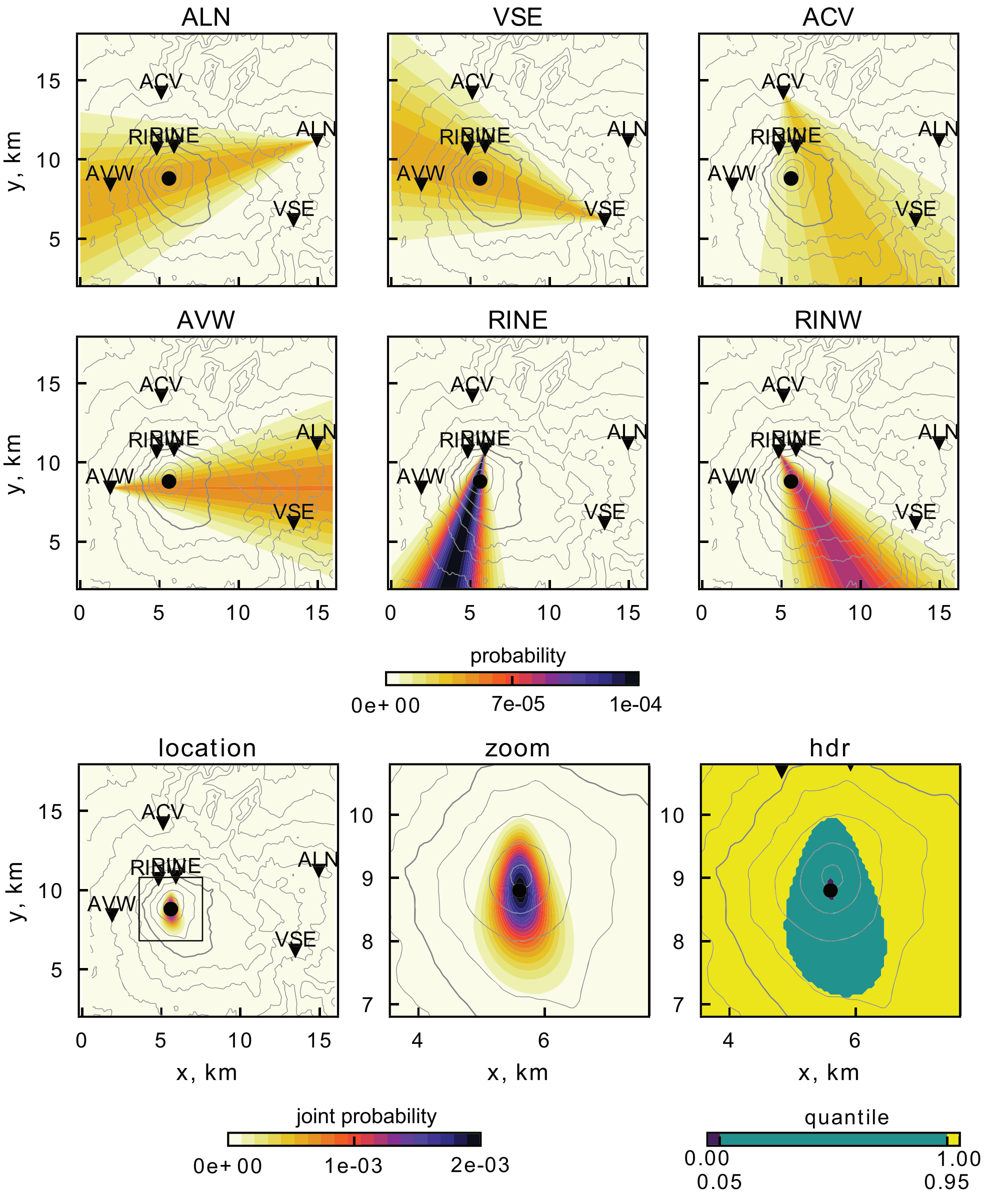

Figure 6. Probability for epicenter locations from each single array (top and middle rows) and normalized superposition of probability density functions indicating the probability of the epicenter from combined arrays. The location procedure can be understood as a superposition of probability density function "beams." Black dot marks maximum of the joint probability. Triangles represent array centers. Topography is indicated in 200-m intervals; 2,000-m contour is highlighted.

interevent tremor. The DOA oscillates around a stable mean value, which is mostly similar at all frequencies. Strong, erratic deviations occur (e.g., at 21.5 min), but their amount is sparse compared to the periods of stable DOA. Moreover, the DOA during these episodes depends stronger on the frequency band. Such fluctuations may occur if reflections or signals from other sources yield more coherent phases in an analysis window. The general stability of the DOA is maintained throughout the whole observation time. Figure 5 also indicates that the DOA is independent of the frequency, while the slowness clearly increases with frequency.

4.2. Epicenter Location

We located the seismic source area by determining the intersection of the beams from our six subarrays. This approach is similar to those described by Almendros et al. (2001a) and Métaxian et al. (2002). The basic idea is that the origin of the signal lies at the intersection of the rays determined by the DOA from multiple

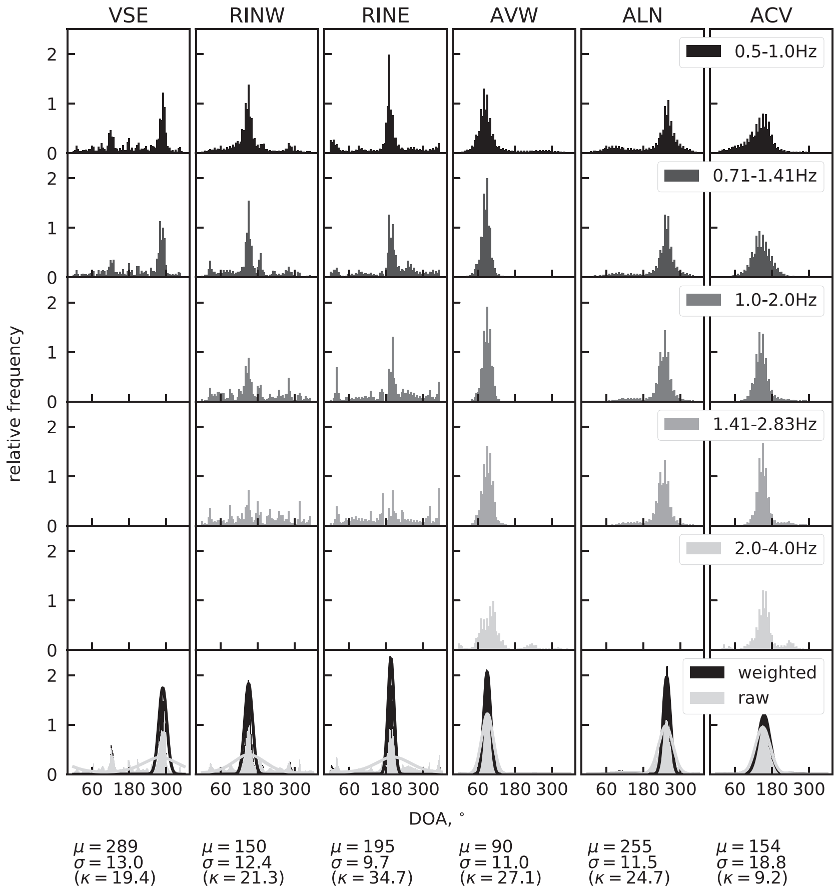

Figure 7. Histograms of directions of arrival. Rows 1–6 show unweighted data for each frequency range available at the corresponding antenna. The last row shows histograms and fitted von-Mises distribution of weighted (black) and unweighted (gray) merged data sets. Shape parameters of the von-Mises distribution are given for weighted merged data set underneath the respective column.

antennas positioned around the source. Given the DOA measurement of an antenna A_i at (x_i, y_i) and an estimate of its uncertainty, we could derive a continuous probability density function (PDF) $f_i(\varphi)$. From this, we determined the likelihood of any direction interval to be the DOA of the detected signal. These likelihoods were backprojected onto a search grid. The joint probability of the intersecting beams is given as

$$p\left(x_j, y_j\right) = \frac{\prod_i^M f_i\left(\varphi_{ij}\right)}{\sum_{l=1}^{N}\left(\prod_i^M f_i\left(\varphi_{ij}\right)\right)} \tag{1}$$

with φ_{ij} being the DOA at A_i for a signal starting at a location $L_j = \left(x_j, y_j\right)$ of the search grid. Instead of the location quality factor proposed by Almendros et al. (2001a) and Métaxian et al. (2002), we normalized the joint probability density (the dividend in equation (1)) by the sum over the entire search grid. This allowed us to interpret the result as an actual probability. The derivation of equation (1) is explained in detail in Appendix A.

In principle, any PDF can serve as f_i. We applied the von-Mises distribution, which is an easy-to-use, normalized approximation of the normal distribution for periodic data (Mardia & Jupp, 1999):

$$f(\varphi|\mu, \kappa) = \frac{e^{\kappa\cos(\varphi-\mu)}}{2\pi I_0(\kappa)}, \qquad \varphi \in [0, 2\pi \tag{2}$$

with I_0 being the modified Bessel function of order 0 and μ and $1/\kappa$ corresponding to mean and variance (σ^2) of the standard normal distribution.

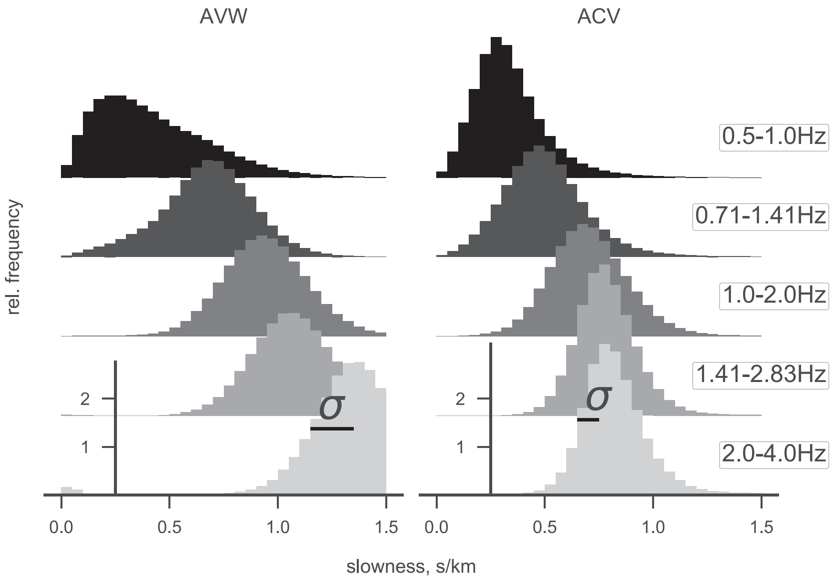

Figure 8. Histograms of slowness values determined by beamforming using the full time range of data. Frequencies are normalized to the total number of observations in the histogram. The slowness clearly increases with signal frequency.

We evaluated equation (1) on a grid of 16 km × 16 km with a sample spacing of $\Delta x = \Delta y = 0.05$ km, including the crater and all arrays. The grid point, which yields the highest probability, is considered as the source.

In order to assess the significance of the outcome of equation (1), we used the concept of "highest-density regions" (HDR; Hyndman, 1996; Kruschke, 2015b). In Bayesian literature it is also referred to as "highest-density interval" (notably for 1-D cases) or "credible interval/region." This region comprises those grid points, which are bound by lines of equal probability such that their sum contributes $100 \cdot q\%$, $q \in [0, 1]$ of the total probability over the whole grid. In other words, the HDR is defined by a contour line of the data, which represents a q-quantile of the probability distribution. The sought-after source location lies with a probability of $100 \cdot q\%$ within that region, given the estimated uncertainties of the measurements. For the computation of the HDR, we used a Python implementation of the algorithm proposed by Kruschke (2015a; www.github.com/aloctavodia/Doing_bayesian_data_analysis).

The projections of the PDFs and the result of their intersection are shown in Figure 6. As described below in detail, the PDFs are representative of the entire recording period. The highest probability is achieved at grid coordinates (5.6 and 9.1 km), corresponding to 71.940°W and 39.4196°S. The source location is thus situated at the northern rim of the summit crater. The area that contributes 95% of the joint probability extends approximately 1,000 m to the north and south of the maximum location and about 500 m to the east and west.

4.3. DOA Determination

The stability of the DOA estimate, regarding frequency and time, is most evident after sorting the DOAs into a histogram (Figure 7). Sections of 1 hr or 1 day always yielded similar distributions of the directions as when using the full time range. The spread of the distributions accommodates the episodic fluctuations of the DOA. The means are independent of the frequency band as shown in Figure 7 (top). Therefore, the data of the available frequency ranges were merged before determining the parameters of equation (2). This minimizes the contribution of the strong perturbations of the DOA (as seen in Figure 5) because they are less consistent regarding frequency. The parameters were then found by fitting the von-Mises distribution to the histogram using a nonlinear least squares solver. The histogram was converted into relative frequencies through division by the number of total observations and normalized so that the sum between $[0, 2\pi[$ is 1. The histograms and fitted von-Mises distributions for the raw DOA data are shown in gray in Figure 7.

We found that the variance of the parameter estimate reduced significantly when the contributions to the histogram were weighted by semblance and sample uncertainty using

$$w = S^n(1 - \frac{\epsilon}{\epsilon_{max}})^m \tag{3}$$

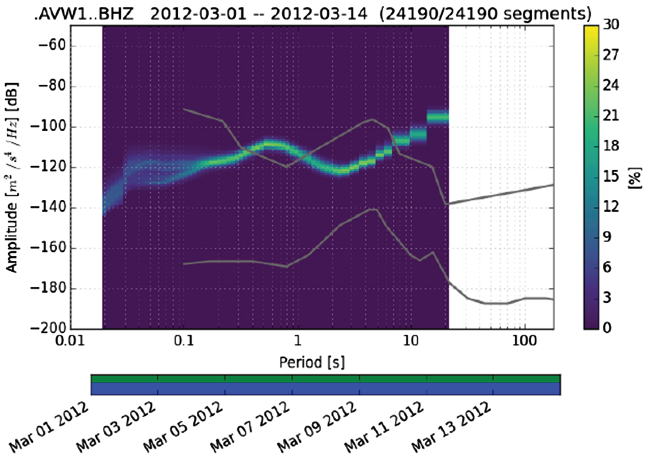

Figure 9. Probabilistic power spectral density for Station AVW1. The color shows the occurrence of each period/amplitude pair in percent. The lower bar plot shows the available data in green and the coverage by the single 100-s-long segments in blue. The gray lines in the diagram represent the low-noise and the high-noise model.

with S being the semblance, $\epsilon_{\max} = \pi$ being the largest expectable error and n, m being scaling factors. We chose $n = 10, m = 10$, which effectively muted data with $S \le 0.8$ when higher semblance values were available but still allowed the method to be applied when the overall semblance was low. The resulting distributions are shown in black in the last row of Figure 7.

Equation (3) is an adaption of the weighting functions used by Almendros et al. (2001a). The semblance was included in order to enhance sequences with high semblances without using an absolute threshold for preselection.

In this way, we extracted DOAs using data of 1- and 24-hr sections as well as the full time period of 9 days. In order to elucidate the relation between the episodic, high-amplitude transients, and the interevent tremor, we separated the data into event and tremor portions based on the energy content of the signal. The histogram analysis yielded the same DOA for both data sets.

4.4. *S* Wave Velocity Profiles From Phase Velocity Dispersion

At Arrays ACV and AVW the slowness shows a distinct dependence on frequency: The maximum in the histogram representation clearly moves toward higher slownesses for increasing frequency (Figure 8), which is a characteristic of surface wave dispersion. Since only vertical components were used in the beamforming analysis, we interpret the detected slowness-frequency relationship as the phase velocity dispersion of Rayleigh waves.

The histogram peaks were attributed to the center frequency of the respective frequency band (the geometric mean of the upper and lower cutoff frequency), while the half-widths at half-maximum served as uncertainty σ_i. From these dispersion curves, S wave velocity-depth functions were determined using the neighborhood algorithm provided by Wathelet (2008). It is a stochastic direct search method where the random generation of new models is guided by the results of previous runs. The quality of a model is assessed by the misfit between the modeled and the observed dispersion curve. It corresponds to the square root of the chi-square test statistic:

$$\chi = \sqrt{\sum_{i=0}^{n_f} \frac{\left(c_{oi} - c_{mi}\right)^2}{\sigma_i^2 n_f}} \tag{4}$$

where n_f is the number of sampled frequencies and c_{oi} and c_{mi} are the observed and modeled velocities in the dispersion relation.

For the inversion, the dispersion curves were resampled to 15 samples between 1.0 and 2.8 Hz on a logarithmic scale. These boundaries correspond to the center frequencies of the second and fifth frequency band. The lowest frequency band of 0.5–1.0 Hz and a center frequency of 0.71 Hz was removed since unrealistically high velocities were required to achieve a reasonable fit. The low-frequency DOAs, however, are consistent with those at higher frequencies indicating that the low-frequency arrivals were emitted from the

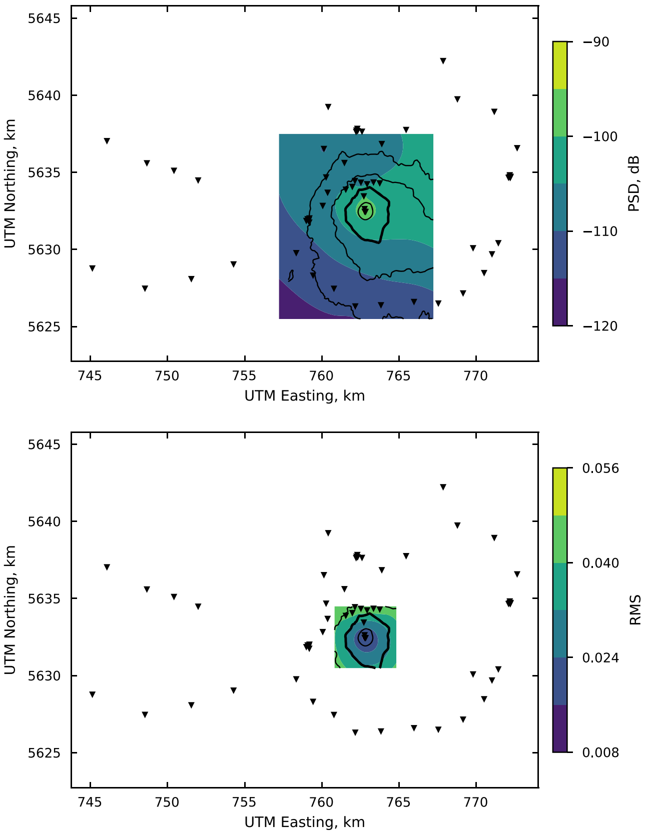

Figure 10. Results of amplitude-based methods. Triangles mark contributing stations. Topography contours are given in black in intervals of 400 m. The 2,200-m contour is highlighted. (top) Amplitude mapping. The maximum marks the epicenter. (bottom) Fitting of amplitude decay. The minimum marks the epicenter. PSD = power spectral density; RMS = root-mean-square.

same source. Their slowness of 0.25 km/s, corresponding to a velocity of 4 km/s, suggests that these arrivals are low-frequency *P* waves.

The formal variables of the inversion are *S* wave and *P* wave velocity, linked by Poisson's ratio, and density (Wathelet, 2008; Wathelet et al., 2004). The model is organized in layers, and layering can be introduced for each of the parameters separately. Each layer is assigned a range for the respective parameters and the thickness. Since the influence of the density is negligible, it was fixed at 2,700 kg/m^3 without layering. For the Poisson's ratio, we restricted the layering to one layer on top of a half-space, with the depth of the top layer coupled to v_S. Expecting unconsolidated material at the surface, we allowed a wider and higher range of 0.25–0.4 for Poisson's ratio and 0.2–0.3 for the half-space (Gercek, 2007). Number and depth of layers for v_P were always analogous to v_S.

To find the basic layer structure, we started the inversion with a model consisting of two layers of constant velocity. Only three constant velocity layers were needed to fit the observed dispersion curve. We also tested models where the constant layer velocities were replaced by velocities with a constant depth gradient. However, given the uncertainties of the measured dispersion curve, no major improvement of the fit could be gained in this way, and the resulting velocity-depth models showed the same basic structure as the velocity models with constant layer velocities. Each input parameter set was tested with five separate runs, with each run converging after 10,200 to 40,800 models.

5. Source Location by Amplitude Decay Analysis (“Amplitude Source Location”)

Battaglia et al. (2003) introduced two methodical variants how the decay of amplitude of a signal along its travel path can be exploited for locating its source: (1) determining the coordinates of the maximum of the

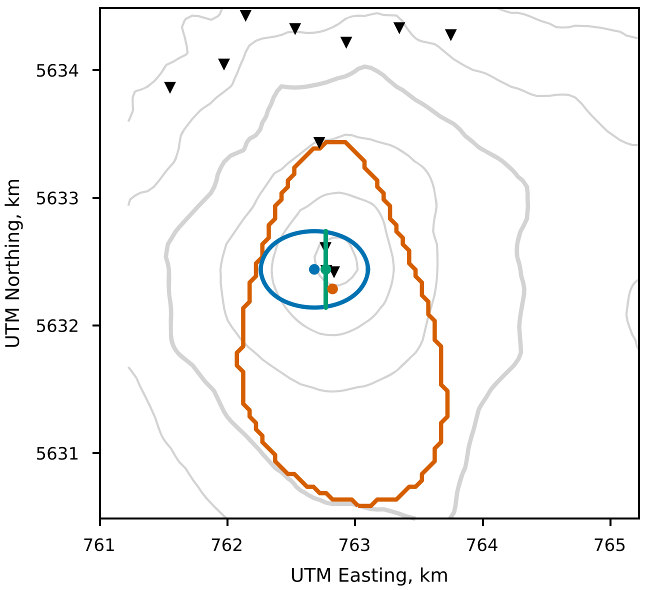

Figure 11. Comparison of the optimum epicenter locations and their confidence intervals based on three different methods (cf. sections 4 and 5): Jackknife estimator and 95% confidence region for amplitude interpolation (green) and amplitude decay fitting (blue); probability maximum and 95% highest-density region for array analysis (orange). Inverted triangles represent stations. Topography contours are given in gray in intervals of 200 m. The 2,200-m contour is highlighted.

amplitude field by interpolating the amplitudes observed at the receivers of a network and (2) performing a grid search for the location, for which the amplitude-distance relation fits a theoretical decay curve best.

For each station, we determined the mean amplitude by computing the probabilistic power spectral density (PPSD) of the signal (McNamara & Buland, 2004). For this purpose, the power spectral density (PSD) is computed for sequential time windows. The resulting large number of PSD estimates allows for a probabilistic evaluation. At each frequency, a histogram of the amplitudes is computed. Hence, the PPSD provides information about how often a combination of frequency and amplitude occurs and therefore allows an interpretation regarding the stability of the frequency content in time.

PPSDs were computed using velocity amplitudes and time windows of 100 s. For each station, all available data were used. The operation time of each station is given in Figure 13 of the supporting information. As shown in the supporting information, we expect correct amplitude determinations for periods between 0.02 and 2.5 s (frequencies of 0.4–50 Hz) after correction for the instrument response.

Figure 9 shows the PPSD at Station AVW1. The prevalent frequency-amplitude-distribution appears as a distinct, narrow band, which indicates a highly stable signal during the whole period of observation. This stability is maintained throughout the network. Therefore, we consider the respective PSDs as representative for the station despite the different record lengths. The broad peak around 0.8 s appears at all stations and its amplitude decays with increasing distance to the summit, suggesting a volcanic origin. Based on this interpretation, we averaged the amplitudes between 1.25 and 3.3 Hz to obtain a representative amplitude of the volcanic signal for the whole recording period. Most stations within 20-km distance to the summit showed a sufficiently high signal-to-noise ratio to be included in the analysis. The 58 stations used for the amplitude source location are marked in Figure 1 in black (or blue and orange, if used before). Site amplification effects were quantified by analyzing the *S* wave amplitudes of regional events. The procedure is described in Appendix B.

For the amplitude interpolation, we used a minimum curvature spline interpolation as proposed by Smith and Wessel (1990) to obtain a map of the amplitudes (Figure 10, top) on a 50-m × 50-m grid. For a point source in a homogeneous medium, amplitude isolines would form concentric circles around a maximum, which represents the epicenter. Deviations from the circular shape reflect either uncertainties in the determined amplitude or spatial variations of geometric spreading or attenuation of the seismic wave. However, even in this case, the location of the amplitude maximum can still be considered as an approximation of the epicenter if the source is situated close to the surface. For deep sources, mislocation due the projection of topographic information on a plane might become problematic if the source is not located underneath the summit. While Battaglia et al. (2003) and Battaglia (2003) interpreted the amplitude maps only qualitatively, we determined the coordinates of the maximum. This enabled us to analyze the accuracy of the result using the jackknife method (Efron & Stein, 1981) as explained below.

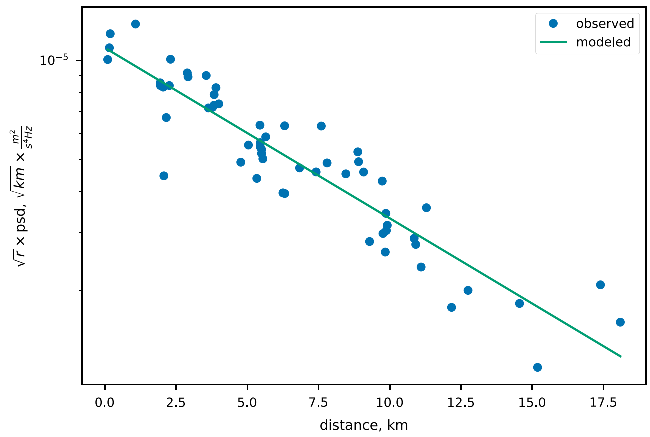

Figure 12. Fit of theoretical and observed amplitude decay for the source coordinates determined by jackknife resampling. psd = power spectral density.

The second variant uses the theoretical description of amplitude decay based on geometrical spreading and absorption (e.g., Aki & Richards, 2002; Stein & Wysession, 2009):

$$A(r) = \frac{A_0}{r^p} \exp(-Cr). \tag{5}$$

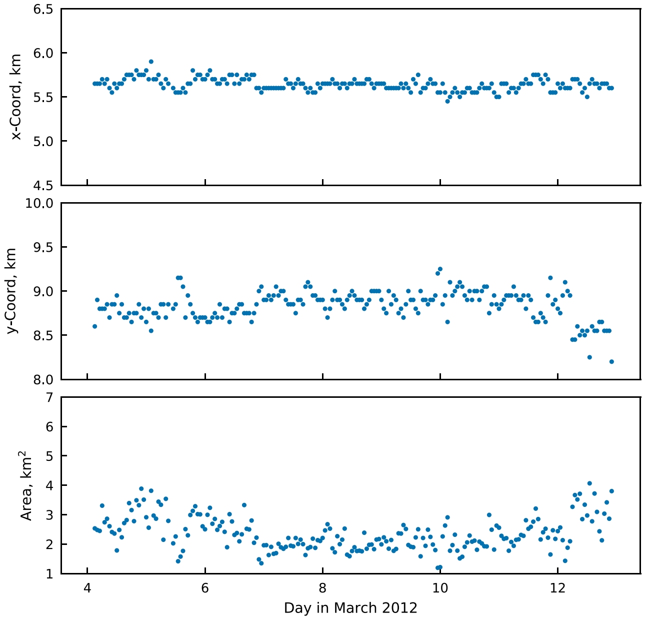

Figure 13. Variation of optimum location parameters with time, determined by array analysis. Parameters were computed for 1-hr segments.

The exponential term describes the anelastic attenuation where the attenuation coefficient is composed of the following:

$$C = \frac{\pi f}{Qv}. \tag{6}$$

Here, f is the frequency, Q is the quality factor, and v is the velocity. The geometrical spreading is given by r^p with $p = 0.5$ for surface waves and $p = 1$ for body waves. Thus, one can perform a spatial grid search to seek the hypocenter where the difference between the observed and theoretical amplitude-distance relation is minimal.

The array analysis (section 4.4 and Figure 8) had shown that the considered wave portions basically consist of Rayleigh waves. This implies that the waves propagate along the Earth's surface and that $p = 0.5$, accordingly. We considered the effect of topography on the travel path by approximating the path by the three-dimensional Euclidean distance between grid point and receiver. Thus, we neglected details of topographic variation between source and receiver. To ensure that this is a reasonable approximation, we computed the path lengths along the topography between the stations and a source at the crater and compared it to the corresponding three- and two-dimensional Euclidean distances. The median of the differences of all stations is 1% and 5% for the 2-D and 3-D cases, respectively. Another consequence of the surface wave assumption is that we implicitly assume that the sources are located near the surface. For the inversion, we used a linearized version of equation (5) with respect to r by multiplying by the spreading factor r^p and taking the natural logarithm (Grazia et al., 2006):

$$\ln\left(A(r)r^p\right) = \ln A_0 - Cr. \tag{7}$$

The slope corresponds to the attenuation coefficient C and the intercept to the logarithm of the initial amplitude A_0. For their determination we used a linear least squares solver which minimizes the Euclidean L2 norm. The residual at any given grid point is the root-mean-square sum of the differences between the observed and modeled left-hand side of equation (7). By this approach, we avoided using a predefined quality factor, as, for example, in Battaglia et al. (2003) or Morioka et al. (2017).

The search grid covered an area of 4 km×4 km, centered on the summit. The distance between the nodes was 50 m, and the vertical source position was given by the topography data. We used a digital elevation model of 90-m resolution, based on SRTM satellite data and provided by Consultative Group on International Agricultural Research-Consortium for Spatial Information (Jarvis et al., 2008). The resulting map of minimum residuals is shown in Figure 10 (bottom). The epicenter is defined by the minimum.

In order to estimate the accuracy of the solution, we applied the jackknife resampling technique (Efron & Stein, 1981) on both methods. Coordinates of the maximum amplitude (interpolation) or minimum residual (grid search) were determined repeatedly by systematically leaving out the ith station. In doing so, we obtained a set of N locations with coordinates $\left(x_{1i}, x_{2i}\right)$ for the amplitude interpolation and the amplitude decay fit, respectively, of which the mean and variance was computed. N is the number of stations.

6. Results

6.1. Location

The source locations and their uncertainties resulting from all three methods are presented in Figure 11. The exact UTM coordinates of the optimum points are listed in Table B1. For the beamforming analysis, these coordinates correspond to the grid cell with the highest single probability. The figure shows the outline of the 95% HDR, while the table lists its approximate extents. For the amplitude methods, the optimum point is the jackknife estimator and the uncertainty is given as twice the standard deviation, derived from the jackknife variance. This corresponds to the extents of the 95% confidence interval of the x and y coordinates, respectively. The differences between the results of all three methods is less than 200 m. The mean epicenter is situated at the geographical coordinates (71.94058°W, 39.42129°S). The epicentral areas determined by the

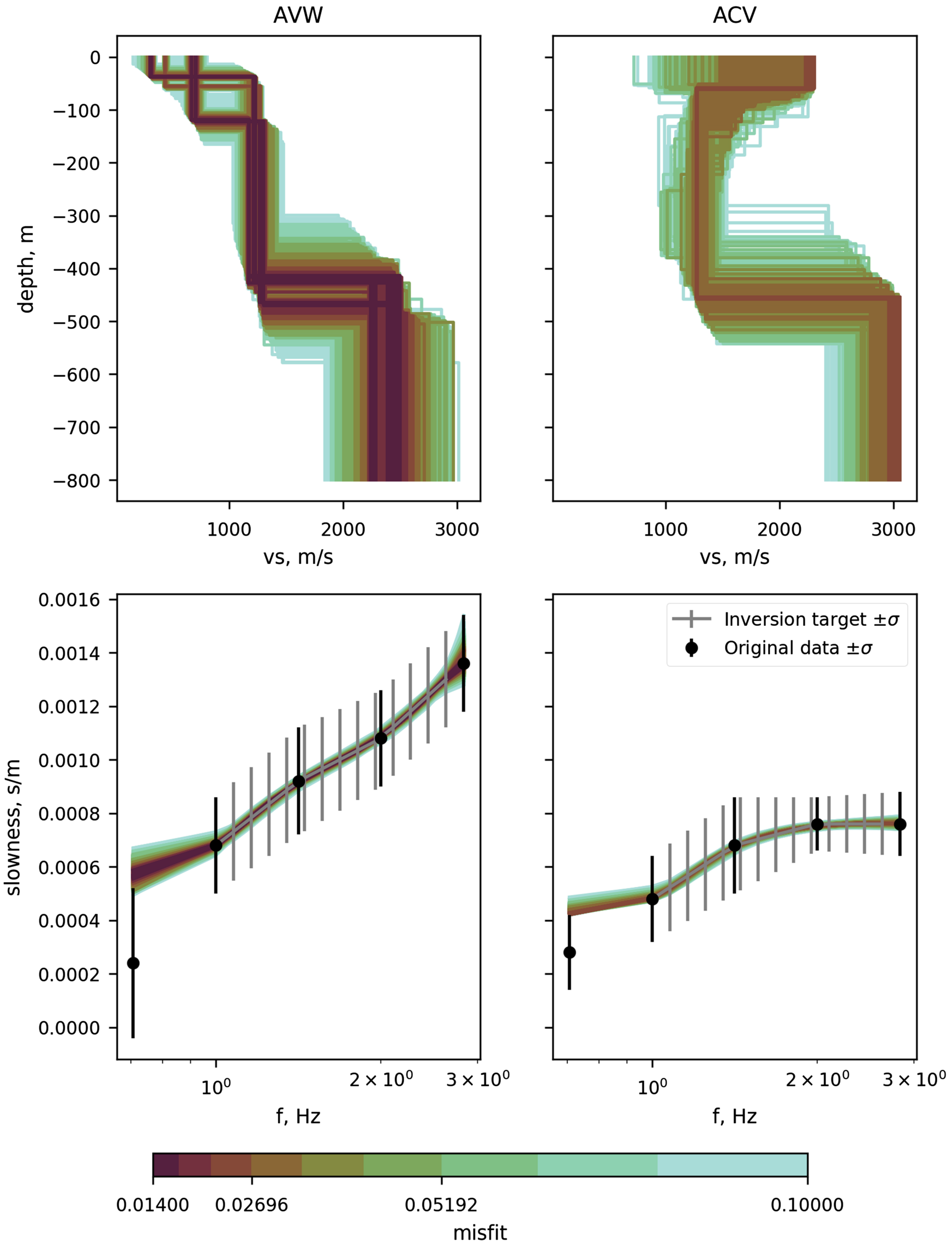

Figure 14. *S* wave velocity profiles (top row) based on inversion of dispersion curves (bottom row) of surface waves at Antennas ACV (right column) and AVW (left column). For the sake of clarity, only every tenth model with a misfit ≤0.1 is shown.

amplitudes methods are situated on the southwestern crater rim, whereas the array analysis positions the source slightly outside the summit crater. Most importantly, the uncertainty intervals overlap completely.

The strong path effects (Figure 3), observed at single event waveforms, and the dependence of slowness on frequency (Figure 8), indicate a prevalence of surface waves in the wavefield. Therefore, we could not deduce a potential source depth.

Figure 12 shows the fit between the observed and modeled amplitudes at the optimum location according to the jackknife test. The mean relative error of the fit is around 2% with a maximum of about 5%. The slope corresponds to an attenuation coefficient of $C = 0.12\,\mathrm{km}^{-1}$. The array analysis yielded slownesses for frequencies around 2 Hz between 0.8 and 1.1 km/s, corresponding to phase velocities of 1.4 and 0.8 km/s, respectively. Using these in equation (6) with f =2.0 Hz results in quality factors Q of 37 and 58.

The DOA values turned out to be very stable during the observation period. Fluctuation occurs on a time scale below hours since histogram analysis on hour- or day-long subsets reveal an equally stable mean DOA. When applied to time segments of 1 hr, the resulting optimum directions μ mostly oscillate within 5° at most around a mean value. Therefore, the corresponding locations vary only slightly within a few grid cells (Figure 13, top and center). The variation in north-south is somewhat larger than in east-west direction, which is in good accordance with the elliptic shape of the HDR. There is no perceptible trend with time, which might be attributed to a moving source. We see the least variation of the coordinates as well as the area of the 95% HDR with time between 7 and 9 March (Figure 13). Similarly, separating the data into "event" and tremor portions based on the energy content of the signal results in the same optimum location.

6.2. Velocity Profiles

The slowness histograms, in contrast to the DOA, vary strongly with frequency. They show a tendency of higher slownesses (lower velocities) toward higher frequencies—a characteristic that indicates surface wave dispersion. The effect is most pronounced at antennas AVW and ACV (Figure 8). Since they are sensitive to the widest frequency range, they are the most suitable for the determination of dispersion curves and velocity profiles.

As representative examples, Figure 14 shows the results for every tenth model that yields a misfit ≤ 0.1. These ensembles comprise the models generated during the five separate, fully independent inversion runs, that yielded the lowest misfits. The velocity profiles (top row) and corresponding dispersion curves (bottom row) are color coded by the misfit. The original dispersion curve and its uncertainties, derived by histogram analysis of the slowness values, is included in black. The interpolated target function used in the inversion is shown in gray. In the following, we primarily refer to the properties of the best fitting models, while the ensemble of possible solutions gives an impression of the spread along the depth and velocity axis, given the uncertainty of the slowness. The models are cut at an arbitrarily chosen depth of 800 m. Note that this deepest layer is the top of the half-space model.

For ACV, a minimum misfit around 0.028 is achieved for a three-layer model. Most remarkably, the best fitting models exhibit a shallow top layer with faster velocities than the one underneath. The ensemble, however, also offers solutions where the lowest velocities are in the surface layer. The inversion converges reliably for five of five independently generated starting models and after 20,400 iterations.

In contrast, AVW exhibits a purely increasing velocity profile while maintaining the three-layer structure. However, the parameter set does not converge as easily. Only 5 out of 20 inversion runs converged at a final misfit around 0.0145 after 20,400 iterations. Yet within these five successful runs, the properties of the top layer remain ambiguous. About 30% of the best models feature a 50-m-thick layer with a velocity of about 370 m/s, whereas the majority yields a 100-m-thick layer with $v_s \approx$700 m/s.

While the velocities in the uppermost 100 m differ greatly, both locations, ACV and AVW, exhibit a layer of 1,100–1,500 m/s in a depth between approximately 100 and 400 m below the surface. The underlying half-space is again slightly different, with velocities around 2,500 m/s for AVW and 3,000 m/s for ACV.

7. Discussion

7.1. Source Location

We applied three different methods to locate the origin of the persistent low-frequency seismicity of Villarrica Volcano in March 2012. All of them yielded an almost identical source region inside the summit crater. This result is in good agreement with the study of Richardson and Waite (2013) who located the source of a repetitive LP event over a time span of three years, including 5–11 March 2012, inside the summit crater. In contrast to their study, we did not locate a selected single event but analyzed the signal as a whole over the full time interval of 9 days. Therefore, it can be concluded that the entire permanent unrest representing the seismicity of Villarrica in the considered time span originated at the summit crater. The way we determined the amplitudes and DOAs for the array method parameters may implicitly enhance the transients due to their higher energy content and slightly better correlation. However, a deliberate separation of high- and low-amplitude portions using the beamforming parameters indicated identical epicenters for the background tremor and the transient events.

The applied location methods imply that the seismic source is at or near the Earth's surface. This assumption is supported by our finding that the observed waveforms are surface waves, from the dispersion of which geologically plausible *S* wave velocity-depth functions could be determined. To further evaluate the assumption of a shallow source depth, we tentatively assumed that the wavefield consists of body waves and repeated the location by amplitude decay fitting. For this test, the distance exponent p in equation (5) was set to 1 and the search space was extended to 3-D. It turned out that the amplitude decay could also be fitted with body waves, while the source location remained close to the surface. We see this as a numerical confirmation of a shallow source depth. Furthermore, the epicentral coordinates determined for the body wave solution deviated by several 100 m from those obtained consistently by array analysis and amplitude interpolation. Therefore, we conclude that the assumptions of surface waves and a shallow source depth are valid. Besides, a shallow source depths favors a strong scattering of the wavefield and, hence, explains the observed significant elongation and alteration of waveforms with source distance better than body waves radiated from a deep source. However, it should be noted that at the lowest frequencies (0.5–1.0 Hz), the velocities obtained by the array analysis were too fast to be surface wave velocities, while the corresponding DOAs—and hence their origin—were similar to those at higher frequencies. Although the slowness would correspond to a plausible *P* wave velocity, we can neither rule out that it results from slower body waves impinging at a steeper angle, which would imply a deeper source.

Regarding the spatial resolution, the probabilistic diagrams (Figures 6, 10, and 11) show that the applied location methods would not be able to separate closely spaced sources ($\leq$100 m). This applies also to a possibly varying source depth inside the conduit. Within these uncertainty limits, we showed that the horizontal coordinates of the signal origin were stable in time and position during our period of observation. Minor fluctuations occurred only on hourly basis. These may be generated numerically by changes in the surrounding noise, which affects the DOA determination but could also be caused by actual variations of the active source.

Our results are strictly valid only for a limited period of observations of 9 days. Therefore, inferences about the source at other time periods should be made with care. However, as we pointed out in section 3.4, comparisons with data from other observation periods suggest that the seismic activity during our campaign was similar in character and frequency to that reported in the previous studies (Calder et al., 2004; Mora-Stock et al., 2014; Ortiz et al., 2003; Palma et al., 2008). Besides, the aforementioned repetitive LP event in the study of Richardson and Waite (2013) occurred over a time span of 3 years, including March 2012, which indicates a certain stability of the volcanic system during that time.

7.2. Attenuation and Scattering

In contrast to other authors using the amplitude source location method (e.g., Battaglia et al., 2003; Kumagai et al., 2011; Morioka et al., 2017), we did not need to predetermine the quality factor due to the linearization of equation (6). Instead, we deduced the damping coefficient from the data during the fitting of the amplitude decay which yielded a quality factor between 37 and 58 for velocities at the frequency of 2 Hz.

Battaglia et al. (2003) used a fixed Q of 50 in their grid search at Kilauea (Hawaii). Using data from Tungurahua and Cotopaxi (both Ecuador), Kumagai et al. (2011) investigated the dependence of the misfit on various given Q and found the lowest residual for $Q = 30$ in the frequency band of 1–6 Hz. Kumagai et al. (2011), Kumagai et al. (2010), and Morioka et al. (2017) point out that the quality factor used in the amplitude source location method is composed of scattering (Q_s) and intrinsic (Q_i) attenuation by $Q^{-1} = Q_s^{-1} + Q_i^{-1}$. Assuming that the wavefield is strongly affected by scattering, Q_s should be low and therefore dominate the total Q. Wegler and Lühr (2001) provided a method to separate scattering and intrinsic attenuation by inverting seismogram envelopes based on the energy diffusion equation. At Merapi (Indonesia), they found $Q_s \approx 2$ and $Q_i \approx 100$ for frequencies as low as 4 Hz. Using the same method, Prudencio et al. (2013) presented mean quality factors of $Q = 35$, $Q_i = 119$, and $Q_s = 45$ for frequencies around 6 Hz at Tenerife Island. Especially, the latter results are fairly similar to our findings. Strong scattering effects become further manifest in the massive alteration of waveforms along their propagation path.

According to Kumagai et al. (2010) and Kumagai et al. (2011) in order for equation (5) to be valid, one must assume isotropic radiation from the source, which is not the case for typical volcanic sources, notably cracks. In order to solve this contradiction, they suggested that scattering effects overprint the initial radiation pattern. To ensure this effect, the amplitude method should be carried out at high frequencies since they are more affected by scattering. At Villarrica, Richardson and Waite (2013) also determined a nearly horizontal, single force source mechanism for their studied LP event, resulting in a strong horizontal component of the signal. Since their observation period partially overlapped with ours, we may assume that at least parts of our data were produced by a similar (or indeed the same) nonisotropic source. Therefore, this problem has to be considered here as well. There are basically three reasons indicating that our results are not affected seriously by radiation patterns: First, as already stressed above, we see indeed evidence of strong scattering effects at the analyzed frequencies. Second, we used a wide and dense station network, which would have revealed systematic distortions of the wavefield due to radiation patterns if they were significant. This is in contrast to Kumagai et al. (2010) and Kumagai et al. (2011) who only used five stations. Third, we used the mean amplitude of a period of 9 days instead of single events. This averaging will compensate radiation bias if the source orientation is rather random than constant over time. Indeed, exemplary particle motion diagrams of the three-component stations revealed that source radiation is variable in time, indicating variation of source types or orientations (see the supporting information).

7.3. Velocity Structure

The velocity-depth profiles, despite the considerable distance between their locations, are remarkably similar below 100 m. The *P* wave tomography of Mora-Stock (2015) proposed a *P* wave velocity of 4.5 km/s at both sites. This value would be consistent with the *S* wave velocity of 1.5 km/s in the middle layer and a Poisson's ratio of 0.25. Métaxian et al. (1997) presented vertical *S* wave velocity models from surface wave inversion for Masaya Volcano (Nicaragua), which are comparable in structure and velocities to ours. They found four layers with thicknesses of around 50–70, 130–170, and 550 m. The *S* wave velocities increase from less than 1.0 km/s at the surface to around 2 km/s above the half-space, starting at 800 m. Velocity-depth functions were obtained at opposite sites of the volcano.

The relatively low velocity values of around 1,500 m/s between 100 and 400 m are typical for moderately consolidated and heterogeneous materials such as deposits from tephra fallouts or pyroclastic density currents. Indeed, exposed deposits from the Chaimilla (3.1 ka), Pucón (3.5 ka), and Licán (13.9 ka) eruptions reveal up to several tens of meters thick layers of ignimbrites, pyroclastic material, and tephra fallout (Costantini et al., 2011; Lohmar et al., 2007; Parejas et al., 2010). These older deposits are widespread around the western and northern flanks (Parejas et al., 2010). Therefore, we may expect a similar velocity structure below the juvenile deposits of recent eruptions.

Velocities around 2,000–3,000 m/s, as found below 400 m, may be attributed to older and more consolidated pyroclasts or ignimbrites.

In contrast, the velocities in the surface layer are notably different between the two sites. The low velocities at the surface at AVW indicate loose and coarse material such as young/fresh pyroclastic deposits, while the high velocities at ACV point to more solid rocks. Corresponding outcrops are found at the respective sites: AVW was placed on rather loose pyroclastic deposits, whereas ACV was situated on a solidified lava flow in the Parque Cuevas Volcánicas.

The colors in Figure 14 represent the misfit between the target dispersion curve and the one yielded by the respective model. Obviously, the dispersion curves even for the least fitting models lie well inside the error bars such that they are to be considered as of similar statistical value. Yet the emanating structure is still well represented by the best fitting models. A dubious case are the velocities of the top layer at ACV, which could also be lower than the ones in the subjacent layer. The fast velocities, however, are backed by the visible geological site properties.

7.4. Implications on the Source Process?

Together with the mild volcanic activity during the campaign, the epicenter inside the summit crater strongly suggests an intimate relation between seismicity and volcanic activity. Despite the considerable number of available studies, little is known about the actual cause of the seismic unrest and the event-like transients at Villarrica. Calder et al. (2004) attributed the transients to small strombolian explosions. Palma et al. (2008) stated a generally good correlation between SO_2 flux and intensity of the seismicity. However, their study is based on only a small number of daily gas observations. They also observed a temporal correlation between bursting bubbles at the lava lake surface and transient seismic events in 2006. Both findings support the general idea that tremor and also LP events are caused by migrating fluids (Chouet, 1996). On the other hand, Goto and Johnson (2011) reported a lack of correlation between the transients in the infrasonic tremor signal and video observations of lake activity in 2010.

The study of Richardson and Waite (2013) used the longest observation time series, in which they identified a repetitive LP waveform that originated in the crater. They interpreted its source-time function as a magma dragging at a horizontal lake bottom. These authors used the term LP events but attributed the investigated signal to seismic and infrasonic emission close to or at the surface of the lava lake. Hence, it is not entirely clear whether their studied event is fundamentally different to our transient events. In the following discussion, we use quotation marks to denote the terminology of Richardson and Waite (2013). Nevertheless, our study likewise located the origin of the seismicity inside the crater. Assuming that the “LPs” of Richardson and Waite (2013) are similar to our transient, our result is in good accordance with theirs.

Moreover, Richardson and Waite (2013) already pointed out that signals may be strongly affected by path effects, and they found an empirical correlation between tremor intensity and the number of detected events. Based on these two findings, they suggested an intimate link between single “LP waveforms” and tremor, such that the tremor signal consists at least partially of overlapping “LP” codas.

Our results support this idea inasmuch as we can confirm the observation that signals evolve from short bursts at the crater into extremely elongated waveforms at a few kilometers distance. Hence, superposition of the signals becomes more and more of an issue up to the point that the discrete impulsive character of the transient events is lost. Signals recorded only at some distance to the crater might be misinterpreted as uniform tremor or LPs.

In addition, we demonstrated that the entirety of the low-frequency signal of Villarrica can be attributed to a confined source region. This could be seen as another indicator for a common source of tremor and events. Yet we have to point out that our methods would probably not resolve too closely spaced sources (≤100 m). This is especially true for different source depths inside the conduit, due to the lack of accurate depth determination.

Finally, not only the location but also the frequency content showed little variation during the period of observation. Nevertheless, we observed significant fluctuations in the character of the seismicity as reported in section 3.4. This suggests at least a close relationship between tremor and transient events. In any case, the stability of the location and frequency imply a sustained generation process of the signal.

On the other hand, Palma et al. (2008) described a complex and not always straightforward interplay of average amplitude level (RSAM) as an indicator of tremor, the number of transient events, degassing, and visible activity of the lava lake. Most importantly, these authors reported a lack of correlation between the event rate and RSAM for the period from November 2004 to April 2005. Calder et al. (2004) even reported the absence of strombolian explosion quakes during a tremor period in August–December 1999. Both observations rather indicate two different source processes for the tremor and the transient events. A more detailed investigation of individual events might provide a better insight into this issue.

8. Conclusion

In early March 2012, Villarrica Volcano showed a continuous low-frequency tremor signal overlain with transient high-amplitude bursts in intervals of approximately 60 s. Using three independent methods (beamforming with intersection, modeling of amplitude decay, and amplitude mapping), we could demonstrate that the epicenters of the signal components as well as of the composite signal as a whole were located in the same area inside the summit crater and close to the Earth's surface. By dispersion analysis it could be shown that the wavefield produced by the seismicity was composed mainly of surface waves. This is consistent with a shallow source depth. The uncertainty of the epicentral coordinates is of the order of some 100 m. Using a moving-window analysis, we could show that the source position was stable during the nine days of observation. The probabilistic evaluation of the power spectral density revealed an equally stable frequency content of the seismic signal. Together with the identical epicenters of transient events and tremor this may indicate an intimate link between the different characteristics of the low-frequency seismic signal. Yet whether this indicates a common (or even identical) source process remains disputable.

Aside from the origin, we obtained *S* wave velocities at the northern and western flank and attenuation parameters of the Villarrica Volcano from the location methods. The velocities of the surface layer are in accordance with the site structures: The low velocities at the western flank correspond to the fresh, poorly consolidated ashes, while the high velocities at the northern location are caused by the lava flow that crosses the Parque Cuevas Volcanicas. Between 100 and 400 m, both locations exhibit very similar velocities around 1,200 m/s, corresponding to pyroclastic deposits and ignimbrites from earlier eruptions. The average seismic quality factor Q is of the order of 50 at around 2 Hz in the uppermost 200 to 300 m.

In comparison with earlier reports on the seismic and volcanic activity of Villarrica (Calder et al., 2004; Ortiz et al., 2003; Palma et al., 2008; Richardson et al., 2014), we believe that our data represent more or less a common behavior of the volcano. Therefore, the source location, which was found in this study, may be considered representative for this type of activity. Nevertheless, we point out that our observation period comprises merely 2 weeks, and hence, inferences to other periods should be made with care. The medium parameters on the other hand are less affected by this limitation unless significant changes happen to the volcanic edifice. They may provide a solid base for a closer look at individual events, which could reveal interesting details about the dynamics inside the conduit.

Appendix A: Probabilistic Intersection

We realize this concept using a probabilistic, Bayesian framework. Given the DOA measurement of a signal by an antenna A_i at $\left(x_i, y_i\right)$ and an estimate of its uncertainty, we may derive a continuous PDF $f_i(\varphi)$. Thus, we know the likelihood of any direction to be the DOA of the detected signal. A signal from a source location $L_j = \left(x_j, y_j\right)$ impinges at A_i from a direction

$$\varphi_{ij} = g\left(x_i, y_i, x_j, y_j\right) = \arctan\left(\frac{x_j - x_i}{y_j - y_i}\right) \tag{A1}$$

This relation allows us to quantify the likelihood that L_j is the source of the signal detected at A_i given that $f_i(\varphi)$ represents the distribution of the results of the DOAs measurements.

Bayes theorem describes the probability of hypothesis H, given an observation O. We postulate that $H: L_j$ is a source of the signal detected at antenna A_i while O: We observed an incoming signal with f_i at A_i.

Eventually, we are going to compare a number of L_j values drawn from a set of N possible locations. We hereby assume that these hypotheses are exclusive (there can be only one source) and exhaustive (one L_j in the set must be the source), so that we need the generalized form of Bayes' theorem (e.g., Bernardo, 2011):

$$P\left(H_j|O\right) = \frac{P\left(O|H_j\right)P\left(H_j\right)}{\sum_{l=1}^{N} P\left(O|H_l\right)P\left(H_l\right)} \tag{A2}$$

Instead of probabilities, one may also use probability densities.

The probability to observe a DOA φ_{ij} if H_j were true is given by f_i; thus,

$$p\left(O|H_j\right) = f_i\left(\varphi_{ij}\right) \tag{A3}$$

Concerning the hypotheses, we may assume $P\left(H_j\right) = const.$ because without any further knowledge all L_j are equally likely to be the source. Consequently, $P\left(H_j\right)$ is eliminated in equation (A2).

Now we want to exploit that we actually have multiple observations O_i of the signal. These observations are statistically independent since one does not require another antenna to detect a signal at A_i. Therefore, the joint probability for making all observations at the same time is given by the product of the individual probabilities and we may extend the above to (Bernardo, 2011)

$$p\left(O_1 \cap \ldots \cap O_M|H_j\right) = \prod_{i}^{M} P\left(O_i|H_j\right) = \prod_{i}^{M} f_i\left(\varphi_{ij}\right) \tag{A4}$$

Table B1
Source Location in UTM Zone 19S

Method	x	y
Array analysis	246,901.7 ± 500 m	5,632,237.7 ± 905 m
Ampl. interpolation	246,851.7 ± 0 m	5,632,387.7 ± 150 m
Ampl. decay	246,761.7 ± 210 m	5,632,387.7 ± 150 m

Moreover, we may treat the set of observations $\{O_i\}$ equivalently to a single observation, so that equation (A2) can be extended by induction and combined with equation (A4) to

$$\begin{aligned} P\left(H_j|O_1 \cap \dots \cap O_M\right) &= \frac{P\left(O_1 \cap \dots \cap O_M|H_j\right)}{\sum_{l=1}^{N} P\left(O_1 \cap \dots \cap O_M|H_l\right)} \\ &= \frac{\prod_i^M P\left(O_i|H_j\right)}{\sum_{l=1}^{N}\left(\prod_i^M P\left(O_i|H_j\right)\right)} \\ &= \frac{\prod_i^M f_i\left(\varphi_{ij}\right)}{\sum_{l=1}^{N}\left(\prod_i^M f_i\left(\varphi_{ij}\right)\right)} \end{aligned} \tag{A5}$$

Appendix B: Site Amplification Estimation

Site amplification factors are needed to correct the amplitudes of the volcanic signals for the influence of near-surface geological layering. We determined a relative site amplification factor for each station following the procedure of Bonilla et al. (1997) for S waves. However, since most of our instruments were single-component sensors, we considered only the vertical component. The procedure was applied to the frequency band between 1 and 3 Hz.

The amplitude spectrum $A(\omega)$ of the observed ground motion of an earthquake can be expressed by

$$A(\omega) = E(\omega) \cdot P(\omega) \cdot S(\omega). \tag{B1}$$

$E(\omega)$ is the amplitude spectrum emitted from the hypocenter of the earthquake (moment, size, and radiation pattern), $P(\omega)$ is the alteration of the amplitude spectrum due to the travel path (e.g., geometrical spreading

Table B2
Regional Events

Event ID	Date	Time	Latitude	Longitude	Depth	ML	Distance (km)
600794002	2012-03-01	06:44:26.53	−38.2115	−73.6291	25.8	4.2	199
604845792	2012-03-01	20:33:28.90	−36.782	−73.57	22.7	3.8	326
604845802	2012-03-02	23:11:19.30	−37.746	−74.745	20.0	3.9	307
600954421	2012-03-03	00:52:38.92	−36.5418	−72.47	51.3	3.9	323
600760711	2012-03-03	22:12:56.11	−35.6975	−72.8917	20.6	4.9	422
600954498	2012-03-03	23:20:14.65	−37.9104	−75.1229	35.0	3.9	324
600760714	2012-03-03	23:43:04.58	−35.7061	−72.8923	20.2	4.8	421
604845822	2012-03-05	08:06:54.37	−36.215	−73.2807	10	3.9	375
600791120	2012-03-09	00:43:33.40	−34.7027	−72.8732	2.6	4.3	531
604845863	2012-03-11	03:30:02.80	−37.562	−74.11	40.4	3.6	280
600778273	2012-03-12	19:37:36.19	−34.961	−71.6532	66.1	4.9	496

Note. Date is formatted as "YYYY-MM-DD."

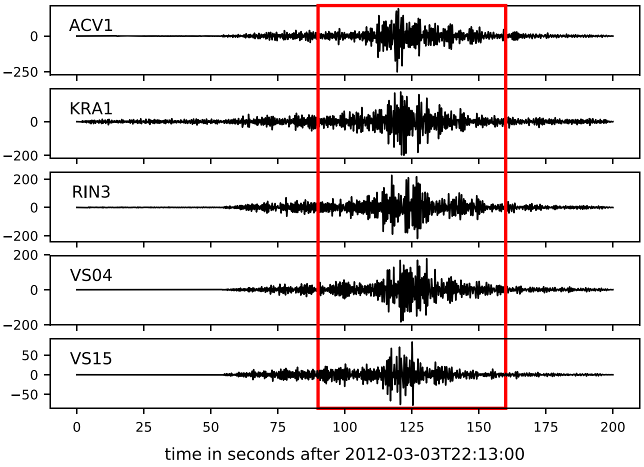

Figure B1. Regional event ML = 4.9 on 3 March 2012 at 22:12:56.11. Waveforms are instrument corrected to ground velocity (μm/s) and filtered with a band pass between 1 and 3 Hz. Red rectangle indicates the time window for the energy determination.

and damping), and $S(\omega)$ is the amplification due to local structure at the recording station (site effect). The site amplification factor relative to a reference station is

$$\frac{S(\omega)}{S_{\mathrm{ref}}(\omega)} = \frac{E_{\mathrm{ref}}(\omega)}{E(\omega)} \cdot \frac{P_{\mathrm{ref}}(\omega)}{P(\omega)} \cdot \frac{A(\omega)}{A_{\mathrm{ref}}(\omega)} \tag{B2}$$

To derive a relative site amplification factor, we selected 11 regional earthquakes (Table B2) showing a strong *S* wave arrival. In the analysis, the following steps were performed: First, the waveform of the vertical component was corrected for the instrument response to obtain the ground motion of the seismic signal. Second, the data were filtered with a band pass between 1 and 3 Hz and the signal energy was determined for a time window around the *S* wave arrival (Figure B1). The energy values were normalized by the signal energy of a reference station (in our case station AVW4) and expressed in decibels.

We assumed that the amplitude spectrum of the incoming wave $E(\omega)$ is approximately the same for all stations, since the radiation angles differ by a maximum of only 3°. This is because lateral extent of the

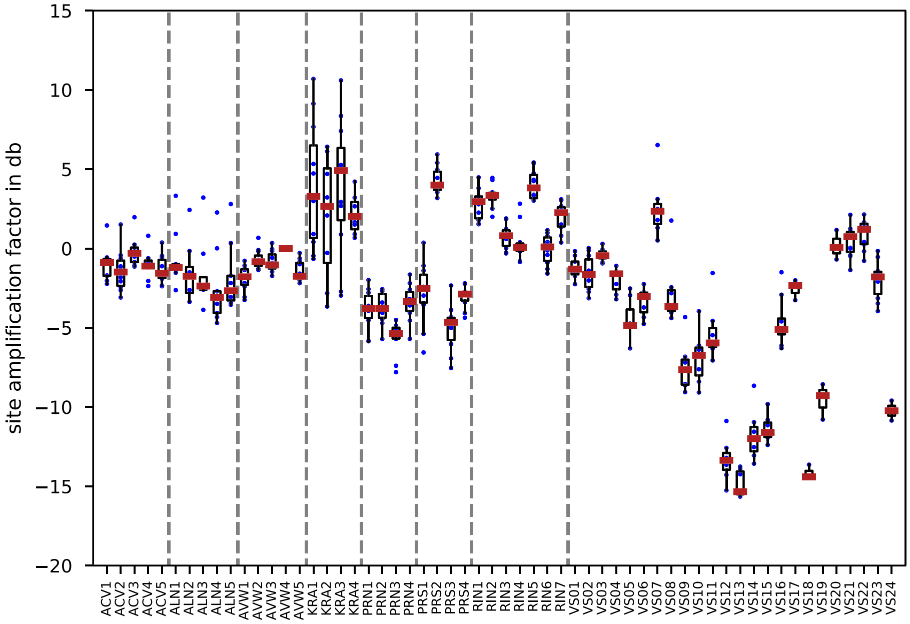

Figure B2. Site amplification factors in decibels. Blue dots indicate every observation, and red stars and the light-blue box the median and the 25–75% quantiles.

network of 20 km is small compared to the epicentral distance of more than 200 km (Table B2). Therefore, the correction for differences in the emitted source spectrum $E_{\text{ref}}(\omega)/E(\omega)$ can be neglected. For the same reason we assumed that the differences in the alteration $P(\omega)$ of the amplitude spectrum caused by differences in the travel path are so small that they can be neglected

The site amplification factor of each station was then determined by computing the median of the normalized energy values derived from the selected eleven regional events (Figure B2). For comparison we also determined the site amplification factors by the more popular coda wave method (e.g., Aki & Chouet, 1975) but found no significant differences between both methods for our data set.

Acknowledgments

We would like to thank the anonymous reviewers for their valuable comments and criticism, which helped to improve the paper. The campaign was funded by the Deutsche Forschungsgemeinschaft Collaborative Research CenterCRC574. The seismometers were provided by the Geophysical Instrument Pool Potsdam (GIPP) of the Deutsches Geoforschungszentrum Potsdam (GFZ). The data are available on request through the GFZ Data Services (http://doi.org/10.5880/GIPP.201202.1). Johanna Lehr receives a PhD-scholarship of Kiel University. Data analysis and visualization was realized by means of Python—notably Obspy, Numpy, Scipy, Matplotlib, and Jupyter—Generic Mapping Tools (GMT) and the Geopsy-package Dinver. We thank the numerous developers for providing of these APIs.

References

Aki, K. (1957). Space and time spectra of stationary stochastic waves, with special reference to microtremors. *Bulletin of the Earthquake Research Institute*, *35*, 415–456.

Aki, K., & Chouet, B. (1975). Origin of coda waves: Source, attenuation, and scattering effects. *Journal of Geophysical Research*, *80*(23), 3322–3342. https//doi.org/10.1029/jb080i023p03322

Aki, K., & Richards, P. G. (2002). *Quantitative Seismology* (2nd ed.). Sausalito, CA: University Science Books.https://ui.adsabs.harvard.edu/abs/2002quse.book.....A

Almendros, J., & Chouet, B. (2003). Performance of the radial semblance method for the location of very, long period volcanic signals. *Bulletin of the Seismological Society of America*, *93*(5), 1890–1903.

Almendros, J., Chouet, B., & Dawson, P. (2001a). Spatial extent of a hydrothermal system at Kilauea Volcano, Hawaii, determined from array analyses of shallow long-period seismicity:, 1. Method. *Journal of Geophysical Research*, *106*(B7), 13,565–13,580. https//doi.org/10.1029/2001jb000310

Almendros, J., Chouet, B., & Dawson, P. (2001b). Spatial extent of a hydrothermal system at Kilauea Volcano, Hawaii, determined from array analyses of shallow long-period seismicity: 2. Results. *Journal of Geophysical Research*, *106*(B7), 13,581–13,597. Retrieved from https//doi.org/10.1029/2001JB000309

Battaglia, J. (2003). Location of seismic events and eruptive fissures on the piton de la fournaise volcano using seismic amplitudes. *Journal of Geophysical Research*, *108*(B8), 2364. Retrieved from https//doi.org/10.1029/2002JB002193

Battaglia, J., Got, J.-L., & Okubo, P. (2003). Location of long-period events below Kilauea Volcano using seismic amplitudes and accurate relative relocation. *Journal of Geophysical Research*, *108*(B12), 2553. https//doi.org/10.1029/2003JB002517

Bernardo, J. M. (2011). Bayesian statistics, *International encyclopedia of statistical science* (pp. 107–133). Berlin, Heidelberg: Springer. Retrieved from https//doi.org/10.1007/978-3-642-04898-2_139

Bonilla, L. F., Steidl, J. H., Lindley, G. T., Tumarkin, A. G., & Archuleta, R. J. (1997). Site amplification in the San Fernando Valley, California: Variability of site-effect estimation using the S-wave, coda, and H/V methods. *Bulletin of the Seismological Society of America*, *87*(3), 710–730.

Calder, E. S., Harris, A. J. L., Peña, P., Pilger, E., Flynn, L. P., Fuentealba, G., & Moreno, H. (2004). Combined thermal and seismic analysis of the Villarrica volcano lava lake, Chile. *Revista geológica de Chile*, *31*(2), 259–272. Retrieved from https//doi.org/10.4067/S0716-02082004000200005

Chouet, B. (1996). Long-period volcano seismicity: Its source and use in eruption forecasting. *Nature*, *380*(6572), 309–316.

Chouet, B., De Luca, G., Milana, G., Dawson, P., Martini, M., & Scarpa, R. (1998). Shallow velocity structure of Stromboli Volcano, Italy, derived from small-aperture array measurements of strombolian tremor. *Bulletin of the Seismological Society of America*, *88*(3), 653–666. Retrieved from https://pubs.geoscienceworld.org/ssa/bssa/article/88/3/653/102728/shallow-velocity-structure-of-stromboli-volcano

Chouet, B., Saccorotti, G., Martini, M., Dawson, P., De Luca, G., & Milana, G. (1997). Source and path effects in the wave fields of tremor and explosions at Stromboli Volcano, Italy. *Journal of Geophysical Research*, *102*(B7), 15,129–15,150. Retrieved from https//doi.org/10.1029/97JB00953

Costantini, L., Pioli, L., Bonadonna, C., Clavero, J., & Longchamp, C. (2011). A Late Holocene explosive mafic eruption of Villarrica Volcano, Southern Andes: The Chaimilla deposit. *Journal of Volcanology and Geothermal Research*, *200*(3), 143–158. Retrieved from https//doi.org/10.1016/j.jvolgeores.2010.12.010

De Barros, L., Bean, C. J., Lokmer, I., Saccorotti, G., Zuccarello, L., O'Brien, G. S., et al. (2009). Source geometry from exceptionally high resolution long period event, observations at Mt Etna during the 2008 eruption. *Geophysical Research Letters*, *36*, L24305. https//doi.org/10.1029/2009GL041273

Di Lieto, B., Saccorotti, G., Zuccarello, L., Rocca, M. L., & Scarpa, R. (2007). Continuous tracking of volcanic tremor at Mount Etna, Italy. *Geophysical Journal International*, *169*(2), 699–705. Retrieved from https//doi.org/10.1111/j.1365-246X.2007.03316.x

Dzierma, Y., Rabbel, W., Thorwart, M., Koulakov, I., Wehrmann, H., Hoernle, K., & Comte, D. (2012). Seismic velocity structure of the slab and continental plate in the region of the 1960 Valdivia (Chile) slip maximum—Insights into fluid release and plate coupling. *Earth and Planetary Science Letters*, *331-332*, 164–176. Retrieved from https//doi.org/10.1016/j.epsl.2012.02.006

Efron, B., & Stein, C. (1981). The jackknife estimate of variance. *The Annals of Statistics*, *9*(3), 586–596. Retrieved from https://www.jstor.org/stable/2240822

Eibl, E. P. S., Bean, C. J., Vogfjörd, K. S., Ying, Y., Lokmer, I., Möllhoff, M., et al. (2017). Tremor-rich shallow dyke formation followed by silent magma flow at Bárdharbunga in Iceland. *Nature Geoscience*, *10*, 299–304.

Ferrazzini, V., Aki, K., & Chouet, B. (1991). Characteristics of seismic waves composing Hawaiian volcanic tremor and gas-piston events observed by a near-source array. *Journal of Geophysical Research*, *96*(B4), 6199–6209. Retrieved from https//doi.org/10.1029/90JB02781

Gercek, H. (2007). Poisson's ratio values for rocks. *International Journal of Rock Mechanics and Mining Sciences*, *44*(1), 1–13. Retrieved from https//doi.org/10.1016/j.ijrmms.2006.04.011

Global Volcanism Program (2013). Villarrica (357120) in Volcanoes of the World, v. 4.8.3. In E. Venzke (Ed.). Smithsonian Institution. Downloaded 23 Oct 2019 (https://volcano.si.edu/volcano.cfm?vn=357120). https://doi.org/10.5479/si.GVP.VOTW4-2013

Global Volcanism Program (2014). Report on Villarrica (Chile). In R. Wunderman (Ed.), *Bulletin of the Global Volcanism Network, 39:3*. Smithsonian Institution. https://doi.org/10.5479/si.GVP.BGVN201403-357120

Global Volcanism Program (2015). Report on Villarrica (Chile). In S. K. Sennert (Ed.), *Weekly Volcanic Activity Report, 25 February-3 March 2015*: Smithsonian Institution and US Geological Survey.

Goto, A., & Johnson, J. B. (2011). Monotonic infrasound and Helmholtz resonance at Volcan Villarrica (Chile). *Geophysical Research Letters*, *38*, L06301. Retrieved from https//doi.org/10.1029/2011GL046858

Grazia, G. D., Falsaperla, S., & Langer, H. (2006). Volcanic tremor location during the 2004 Mount Etna lava effusion. *Geophysical Research Letters*, *33*, L04304. https//doi.org/10.1029/2005gl025177

Havskov, J., & Alguacil, G. (2004). *Instrumentation in earthquake seismology* (Vol. 358). Switzerland: Springer.

Hilbert, H.-S. (2015). Die Übertragungsfunktion von Geophonen: Eigenschaften und Restituierbarkeit (Bachelor's thesis), Kiel University.

Hyndman, R. J. (1996). Computing and graphing highest density regions. *The American Statistician*, *50*(2), 120–126. Retrieved from https//doi.org/10.2307/2684423

Jarvis, A., Guevara, E., Reuter, H. I., & Nelson, A. D. (2008). Hole-filled SRTM for the globe Version 4 (*SRTM 90m Database*): International Centre for Tropical Agriculture (CIAT). Retrieved from http://srtm.csi.cgiar.org (available from http://srtm.csi.cgiar.org/).

Kruschke, J. K. (2015a). Chapter 25—Tools in the trunk, *Doing Bayesian data analysis* (2nd ed., pp. 721–736). Boston: Academic Press. Retrieved from https//doi.org/10.1016/B978-0-12-405888-0.00025-8

Kruschke, J. K. (2015b). Chapter 4—What is this stuff called probability? *Doing Bayesian data analysis* (2nd ed.). Boston: Academic Press. Retrieved from https//doi.org/10.1016/B978-0-12-405888-0.00004-0

Kumagai, H., Nakano, M., Maeda, T., Yepes, H., Palacios, P., Ruiz, M., et al. (2010). Broadband seismic monitoring of active volcanoes using deterministic and stochastic approaches. *Journal of Geophysical Research*, *115*, B08303. Retrieved from https//doi.org/10.1029/2009JB006889

Kumagai, H., Saito, T., O'Brien, G., & Yamashina, T. (2011). Characterization of scattered seismic wavefields simulated in heterogeneous media with topography. *Journal of Geophysical Research*, *116*, B03308. Retrieved from https//doi.org/10.1029/2010JB007718

Lohmar, S., Parada, M., Gutirrez, F., Robin, C., & Gerbe, M. C. (2012). Mineralogical and numerical approaches to establish the pre-eruptive conditions of the mafic Licán Ignimbrite, Villarrica Volcano (Chilean Southern Andes). *Journal of Volcanology and Geothermal Research*, *235-236*, 55–69. Retrieved from https//doi.org/10.1016/j.jvolgeores.2012.05.006

Lohmar, S., Robin, C., Gourgaud, A., Clavero, J., Parada, M. A., Moreno, H., et al. (2007). Evidence of magma-water interaction during the 13,800 years BP, explosive cycle of the Licán Ignimbrite, Villarrica Volcano, (Southern Chile). *Revista geológica de Chile*, *34*, 233–247. Retrieved from http://www.scielo.cl/scielo.php?script=sci_arttext&pid=S0716-02082007000200004&nrm=iso

Mardia, K. V., & Jupp, P. E. (1999). Basic concepts and models, *Directional statistics directional statistics* (pp. 25–56). Hoboken, New Jersey: John Wiley & Sons, Inc.Retrieved from https//doi.org/10.1002/9780470316979.ch3

McNamara, D. E., & Buland, R. P. (2004). Ambient noise levels in the continental United States. *Bulletin of the Seismological Society of America*, *94*(4), 1517–1527. Retrieved from https//doi.org/10.1785/012003001

Métaxian, J.-P., Lesage, P., & Dorel, J. (1997). Permanent tremor of Masaya Volcano, Nicaragua: Wave field analysis and source location. *Journal of Geophysical Research*, *102*(B10), 22,529–22,545. Retrieved from https//doi.org/10.1029/97JB01141

Métaxian, J.-P., Lesage, P., & Valette, B. (2002). Locating sources of volcanic tremor and emergent events by seismic triangulation: Application to Arenal volcano, Costa Rica. *Journal of Geophysical Research*, *107*(B10), 2243. Retrieved from https//doi.org/10.1029/2001JB000559

Mora-Stock, C. (2015). Seismic structure and seismicity of the Villarrica Volcano, (Southern Central Chile) (Phd Thesis), Christian-Albrechts-Universität zu Kiel. Retrieved from http://macau.uni-kiel.de/receive/dissertation_diss_00017649

Mora-Stock, C., Thorwart, M., Wunderlich, T., Bredemeyer, S., Hansteen, T. H., & Rabbel, W. (2014). Comparison of seismic activity for Llaima and Villarrica Volcanoes, prior to and after the Maule 2010 earthquake. *International Journal of Earth Sciences*, *103*(7), 2015–2028.

Moreno, H., & Clavero, J. (2006). Mapa geológico del área del volcán Villarrica, Regiones de la, Araucanía y de los Lagos (escala 1:50.000) (*Carta Geológica de Chile, Série Geológia Básica, No., 98, 35*): Servicio Nacional de Geología y Minería. Retrieved from http://www.sernageomin.cl/volcan-villarrica/

Morioka, H., Kumagai, H., & Maeda, T. (2017). Theoretical basis of the amplitude source location method for volcano-seismic signals. *Journal of Geophysical Research: Solid Earth*, *122*, 6538–6551. Retrieved from https//doi.org/10.1002/2017JB013997

Ohminato, T., Chouet, B. A., Dawson, P., & Kedar, S. (1998). Waveform inversion of very long period impulsive signals associated with magmatic injection beneath Kilauea volcano, Hawaii. *Journal of Geophysical Research*, *103*(B10), 23,839–23,862. https//doi.org/10.1029/98jb01122

Ortiz, R., Moreno, H., García, A., Fuentealba, G., Astiz, M., Peña, P., et al. (2003). Villarrica Volcano (Chile): Characteristics of the volcanic tremor, and forecasting of small explosions by means of a material failure, method. *Journal of Volcanology and Geothermal Research*, *128*(1), 247–259. Retrieved from https//doi.org/10.1016/S0377-0273(03)00258-0

Palma, J. L., Calder, E. S., Basualto, D., Blake, S., & Rothery, D. A. (2008). Correlations between SO_2 flux, seismicity, and outgassing activity at the open vent of Villarrica Volcano, Chile. *Journal of Geophysical Research*, *113*, B10201. Retrieved from https//doi.org/10.1029/2008JB005577

Parejas, C. S., Druitt, T. H., Robin, C., Moreno, H., & Naranjo, J.-A. (2010). The Holocene Pucón eruption of Volcán Villarrica, Chile: Deposit architecture and eruption chronology. *Bulletin of Volcanology*, *72*(6), 677–692. Retrieved from https//doi.org/10.1007/s00445-010-0348-9

Pavlis, G. L., & Vernon, F. L. (1994). Calibration of seismometers using ground noise. *Bulletin of the seismological society of America*, *84*(4), 1243–1255. Retrieved from https://pubs.geoscienceworld.org/ssa/bssa/article/84/4/1243/119878/calibration-of-seismometers-using-ground-noise

Prudencio, J., Del Pezzo, E., Garcíá-Yeguas, A., & Ibáñez, J. M. (2013). Spatial distribution of intrinsic and scattering seismic attenuation in active volcanic islands—I: Model and the case of Tenerife Island. *Geophysical Journal International*, *195*(3), 1942–1956. Retrieved from https//doi.org/10.1093/gji/ggt361

Rabbel, W., & Thorwart, M. (2019). Villarrica Tomography (VITO) (dataset). GFZ Data Services. https//doi.org/10.5880/GIPP.201202.1

Richardson, J. P., & Waite, G. P. (2013). Waveform inversion of shallow repetitive long period events at Villarrica, Volcano, Chile. *Journal of Geophysical Research: Solid Earth*, *118*, 4922–4936. Retrieved from https//doi.org/10.1002/jgrb.50354

Richardson, J. P., Waite, G. P., & Palma, J. L. (2014). Varying seismic-acoustic properties of the fluctuating lava lake, at Villarrica Volcano, Chile. *Journal of Geophysical Research: Solid Earth*, *119*, 5560–5573. Retrieved from https//doi.org/10.1002/2014JB011002

Ripepe, M., Marchetti, E., Bonadonna, C., Harris, A. J. L., Pioli, L., & Ulivieri, G. (2010). Monochromatic infrasonic tremor driven by persistent degassing and convection at Villarrica Volcano, Chile. *Geophysical Research Letters*, *37*, L15303. Retrieved from https//doi.org/10.1029/2010GL043516

Saccorotti, G., Chouet, B., & Dawson, P. (2001). Wavefield properties of a shallow long-period event and tremor at, Kilauea Volcano, Hawaii. *Journal of Volcanology and Geothermal Research*, *109*(1), 163–189. Retrieved from https//doi.org/10.1016/S0377-0273(00)00310-3

Saccorotti, G., Maresca, R., & Pezzo, E. D. (2001). Array analyses of seismic noise at Mt. Vesuvius Volcano, Italy. *Journal of Volcanology and Geothermal Research*, *110*(1-2), 79–100. https//doi.org/10.1016/s0377-0273(01)00204-9

Schweitzer, J., Fyen, J., Mykkeltveit, S., & Kværna, T. (2012). Seismic arrays. In P. Bormann (Ed.), *New Manual of Seismological Observatory Practice 2 (NMSOP-2)* (pp. 1–80). Potsdam: Deutsches GeoForschungsZentrum GFZ. Retrieved from https//doi.org/10.2312/GFZ.NMSOP-2_ch9

Smith, W. H. F., & Wessel, P. (1990). Gridding with continuous curvature splines in tension. *GEOPHYSICS*, *55*(3), 293–305. Retrieved from https//doi.org/10.1190/1.1442837

Stein, S., & Wysession, M. (2009). *An introduction to seismology, earthquakes, and Earth structure*. Hoboken: John Wiley & Sons.

The ObsPy Development Team (2017). ObsPy 1.1.0. Retrieved from https//doi.org/10.5281/zenodo.165135

Wassermann, J. (1997). Locating the sources of volcanic explosions and volcanic tremor at Stromboli Volcano (Italy) using beam-forming on diffraction hyperboloids. *Physics of the Earth and Planetary Interiors*, *104*(1-3), 271–281. Retrieved from https//doi.org/10.1016/s0031-9201(97)00041-1

Wathelet, M. (2008). An improved neighborhood algorithm: Parameter conditions and dynamic scaling. *Geophysical Research Letters*, *35*, L09301. https//doi.org/10.1029/2008gl033256

Wathelet, M., Jongmans, D., & Ohrnberger, M. (2004). Surface-wave inversion using a direct search algorithm and its application to ambient vibration measurements. *Near Surface Geophysics*, *2*(4), 211–221. https//doi.org/10.3997/1873-0604.2004018

Wegler, U., & Lühr, B. G. (2001). Scattering behaviour at Merapi volcano (Java) revealed from an, active seismic experiment. *Geophysical Journal International*, *145*(3), 579–592. https//doi.org/10.1046/j.1365-246x.2001.01390.x

Wielandt, E., & Bormann, P. (2002). Seismic sensors and their calibration. *New Manual of Seismological Observatory Practices*, *1*, 46.

Wright, R., Flynn, L. P., Garbeil, H., Harris, A. J. L., & Pilger, E. (2004). MODVOLC: Near-real-time thermal monitoring of global volcanism. *Journal of Volcanology and Geothermal Research*, *135*(1-2), 29–49. https//doi.org/10.1016/j.jvolgeores.2003.12.008

Zuccarello, L., Burton, M. R., Saccorotti, G., Bean, C. J., & Patanè, D. (2013). The coupling between very long period seismic events, volcanic tremor, and degassing rates at Mount Etna volcano. *Journal of Geophysical Research: Solid Earth*, *118*, 4910–4921. Retrieved from https//doi.org/10.1002/jgrb.50363

Zuccarello, L., Paratore, M., La Rocca, M., Ferrari, F., Messina, A., Branca, S., & García, L. (2016). Shallow velocity model in the area of Pozzo Pitarrone, Mt. Etna, from single station, array methods and borehole data. *Annals of Geophysics*, *59*(4), 0433. Retrieved from https//doi.org/10.4401/ag-7086